ACS OMEGA

http://pubs.acs.org/journal/acsodf

Article

Theoretical Modeling (Sparkle RM1 and PM7) and Crystal Structures of the Luminescent Dinuclear Sm(III) and Eu(III) Complexes of 6,6,7,7,8,8,8- Heptafluoro-2,2-dimethyl-3,5-octanedione and 2,3-Bis(2-pyridyl)pyrazine: Determination of Individual Spectroscopic Parameters for Two Unique Eu^{3+} Sites

Aabid Bashir Ganaie and Khalid Iftikhar*

Cite This: *ACS Omega* 2021, 6, 21207−21226

Read Online

ACCESS | Metrics & More | Article Recommendations | Supporting Information

ABSTRACT: Heteroleptic homo dinuclear complexes $[Sm(fod)_3(\mu\text{-bpp})Sm(fod)_3]$ and $[Eu(fod)_3(\mu\text{-bpp})Eu(fod)_3]$ and their diamagnetic analogue $[Lu(fod)_3(\mu\text{-bpp})Lu(fod)_3]$ (fod is the anion of 6,6,7,7,8,8,8- heptafluoro-2,2-dimethyl-3,5-octanedione (Hfod) and bpp is 2,3-bis(2-pyridyl)pyrazine) are synthesized and thoroughly characterized. The lanthanum gave a 1:1 adduct of $La(fod)_3$ and bpp with the molecular formula of $[La(fod)_3bpp]$. The ^1H NMR and ^1H-^1H COSY spectra of the complexes were used to assign the proton resonances. In the case of paramagnetic Sm^{3+} and Eu^{3+} complexes, the methine (of the fod moiety) and the bpp resonances are shifted in the opposite direction and the paramagnetic shifts are dipolar in nature, which decrease with increasing distance of the proton from the metal ion. The single-crystal X-ray analyses reveal that the complexes (Sm^{3+} and Eu^{3+}) are dinuclear and crystallize in the triclinic *P*1 space group. Each metal in a given complex is eight coordinate by coordinating with six oxygen atoms of three fod moieties and two nitrogen atoms of the bpp. Of the two metal centers, in a given complex, one has a distorted square antiprism arrangement and the other acquires a distorted dodecahedron geometry. The Sparkle RM1 and PM7 optimized structures of the complexes are also presented and compared with the crystal structure. Theoretically observed bond distances are in excellent agreement with the experimental values, and the RMS deviations for the optimized structures are 2.878, 2.217, 2.564, and 2.675 Å. The photophysical properties of Sm^{3+} and Eu^{3+} complexes are investigated in different solvents, solid, and PMMA-doped thin hybrid films. The spectroscopic parameters (the Judd−Ofelt intensity parameters, radiative parameters, and intrinsic quantum yield) of each Eu^{3+} sites are calculated using the overlap polyhedra method. The theoretically obtained parameters are close to the experimental results. The lifetime of the excited state is 38.74 μs for Sm^{3+} and 713.62 μs for the Eu^{3+} complex in the solid state.

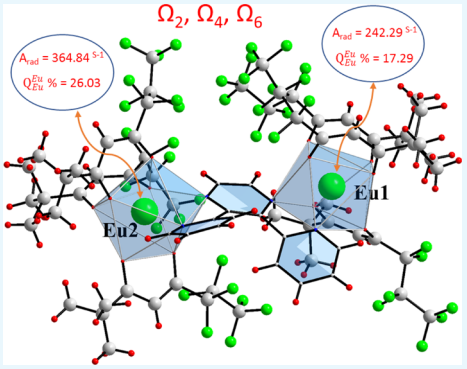

1. INTRODUCTION

The luminescence of lanthanides being unique in its own nature has made them applicable as lasers,[1] sensors,[2,3] luminescent materials,[4−8] luminescence based tools for the investigation of cellular environments,[9] and solar energy conversion devices.[10,11] The lanthanide emission bands are very sharp and exhibit long emission decay times.[12] The direct optical excitation of lanthanide metal ions results in poor emission quantum yields due to lower absorptivity coefficients in the UV−Visible spectrum. To overcome this problem, the indirect excitation through the organic ligands is used. The choice of the organic ligand for light harvesting and then efficiently transferring the energy to the metal ion is the key for achieving higher quantum yields (antenna effect).[13,14] Luminescence can also be intensified by tuning the triplet state of the coordinating ligands to provide a suitable energy gap for effective energy transfer from the triplet state of the ligand to the emissive level of lanthanide ions.[15] Of the plethora of the ligands used as sensitizers, β-diketones are one of the most effective ligands[16] for the sensitization of the lanthanide ions since the β-diketone derivatives are easy to prepare, have greater stability, and present noticeable luminescence properties.[17,18] The fluorines in the fluorinated β-diketones also enhance the overall quantum yield by reducing the non-radiative decay occurring via high energy C−H/N−H vibrations by replacing them with lower energy

Received: December 8, 2020
Accepted: June 14, 2021
Published: August 12, 2021

https://doi.org/10.1021/acsomega.0c05976
ACS Omega 2021, 6, 21207−21226

C−F vibrations.[17−19] The fluorinated β-diketone complexes possess greater oxidative and thermal stability (evaporable) while presenting applications as single molecule magnets[20] and electroluminescent devices.[21,22] The lanthanide tris β-diketone being coordinatively unsaturated are highly reactive and readily coordinate with the approaching ancillary ligand. The ancillary ligands are proficient in suppression of radiation less transitions by replacing the water molecules in the coordination sphere and therefore intensify the overall luminescence. Voluminous combinations of β-diketones and ancillary ligands have been studied for the subject of luminescence.[16−22] Along the same lines, our group hitherto has synthesized and studied many mononuclear,[22−24] dinuclear,[25] and hetero-dinuclear[26] complexes for the purposes of fabricating OLEDs and luminescent materials resulting from various combinations of different fluorinated β-diketones and several ancillary ligands. The luminescence of samarium (pink/orange) and europium (red) complexes/materials has been studied extensively among the lanthnides.[5,17,18,27−31] Lately, there are excellent reports of samarium and europium complexes/materials with exemplary luminescence properties.[14,27−30,32−34]

Alongside the evolution of single-crystal X-ray as a reliable tool for the structure determination, the theoretical techniques like *ab initio* methodologies or density functional theory[35] and the semiempirical tools like Sparkle have also been evolved.[36,37] The semiempirical Sparkle RM1[36] and PM7[37] have proven successful in prediction of the ground state geometries of the lanthanide complexes. The semiempirical models not only predict geometries for mono-,[38,39] di-,[40] tri-, and polynuclear lanthanide complexes,[41,42] they also can divine it for more complicated structures like lanthanide organic frameworks in a reasonable time.[43−45] The theoretical estimation of spectroscopic parameters[46−48] for simple mononuclear complexes using single crystal or optimized structure is routinely used.[43] However, the determination of Judd−Ofelt intensity parameters[49,50] for individual metal centers for a polynuclear complex by a classical method provides inconsistent results and, to overcome this problem, Frerie and coworkers[42] have developed some engrossing theoretical procedures. So, of the reported procedures, the overlap polyhedra method (OPM) has been successfully used to calculate the individual parameters for the two[45] and three[48] unique centers present in the lanthanide complexes.

There are many reports of transition metal complexes[51−58] where 2,3-bis(2-pyridyl) pyrazine (bpp) acts as a bridging ligand, however, a few reports in the case of mixed transition and lanthanide metal complexes.[59,60] Only a handful of lanthanide complexes are reported in the literature[61,62] in which the polyazine ligand bpp acts as a bridge between two lanthanide centers. The homo-dinuclear heavier lanthanide complexes of the $[Ln(tta)_3]_2$bpp (Ln = Eu^{3+}, Gd^{3+}, and Er^{3+}) where bpp acts as a bridging ligand are reported in the literature.[61,62]

In the present paper, we report both chemical and photo luminescence properties of newly synthesized heteroleptic dinuclear complexes of Sm^{3+} and Eu^{3+} containing a highly fluorinated asymmetric β-diketone 6,6,7,7,8,8,8-heptafluoro-2,2-dimethyl-3,5-octadione (Hfod) and 2,3-bis(2-pyridyl) pyrazine (bpp), which acts as a bridging ancillary ligand. The complexes are thoroughly characterized. The structure of the complexes was elucidated experimentally by single-crystal X-ray diffraction (XRD) and theoretically by Sparkle/RM1[36] and PM7[37] models. The shape analysis of the structure of the complexes is also performed to assign the geometries of the coordinate polyhedra around each metal center in the complex (Sm^{3+} and Eu^{3+}). The photoluminescence study of the complexes was conducted in solid, solution, and PMMA-doped hybrid films. The Judd−Ofelt parameters, radiative and non-radiative decay rates, and intrinsic quantum yields for the two unique europium centers of the $[Eu(fod)_3(\mu\text{-bpp})Eu(fod)_3]$ complex are calculated using the overlap polyhedra method (OPM).[42]

2. RESULTS AND DISCUSSION

2.1. Experimental (Single-Crystal X-ray Analysis) and Theoretical Structure Elucidation. Pure crystals suitable for single-crystal X-ray analysis were obtained by slow evaporation of ethanol solution of isolated complexes. The single-crystal X-ray analysis data is presented in Table 1. The single-crystal structure analysis reveals that Sm^{3+} and Eu^{3+} complexes are dinuclear, in which the two metal centers are bridged by the bpp ligand. Both the complexes crystallize in the triclinic *P*1 space group and have similar unit cell dimensions. Each unit cell contains two independent moieties of $[Ln(fod)_3(\mu\text{-bpp})Ln(fod)_3]$ (Ln = Sm and Eu). These complexes are isomorphous, in which each metal center is surrounded by six oxygen atoms (from three fod ligands) and two nitrogen atoms (from the bpp ligand) resulting in an eight-coordinate structure (Figures 1 and 2). Each metal center in these complexes (Sm and Eu) is coordinated to one pyridyl and one pyrazine nitrogen on each side of bpp. The metal−N and metal−O bond distances are presented in Table 2. It is interesting to mention that the average Eu−O (2.35 Å) and Eu−N (2.62 Å) bond distances are shorter than Sm−O (2.38 Å) and Sm−N (2.65 Å), which could be the result of the smaller size of Eu^{3+} ions. The intermetallic distances between the two metal centers are 7.96 Å (Sm−Sm) and 7.90 Å (Eu−

Table 1. Crystal Structure Data and Structure Refinement of Complexes

	$[Sm(fod)_3(\mu\text{-bpp})Sm(fod)_3]$	$[Eu(fod)_3(\mu\text{-bpp})Eu(fod)_3]$
CCDC number	1956378	1956379
empirical formula	$C_{74}H_{70}F_{42}N_4O_{12}Sm_2$	$C_{74}H_{70}F_{42}N_4O_{12}Eu_2$
formula weight	2306.06	2309.28
temperature	100 K	100 K
wavelength	0.71073 Å	0.71073 Å
crystal system	triclinic	triclinic
space group	*P*1	*P*1
unit cell dimensions	a = 12.384 Å, α = 103.858	a = 12.322 Å, α = 103.841°
	b = 19.821 Å, β = 90.682°	b = 19.694 Å, β = 90.859°
	c = 19.834 Å, γ = 102.420°	c = 19.714 Å, γ = 102.307°
volume	4606 $Å^3$	4527 $Å^3$
Z	2	2
density	1.663g cm^{-3}	1.694g cm^{-3}
absorption coefficient	1.404 mm^{-1}	1.516 mm^{-1}
F(000)	2280	2284.0
reflections collected	28956	27838
completeness to theta = 30.840°	95.2%	96.7%
final *R* indices [I > 2sigma(I)]	R_1 = 0.0878, wR_2 = 0.2747	R_1 = 0.0883, wR_2 = 0.2317
S	1.037	1.081

https://doi.org/10.1021/acsomega.0c05976
ACS Omega 2021, 6, 21207−21226

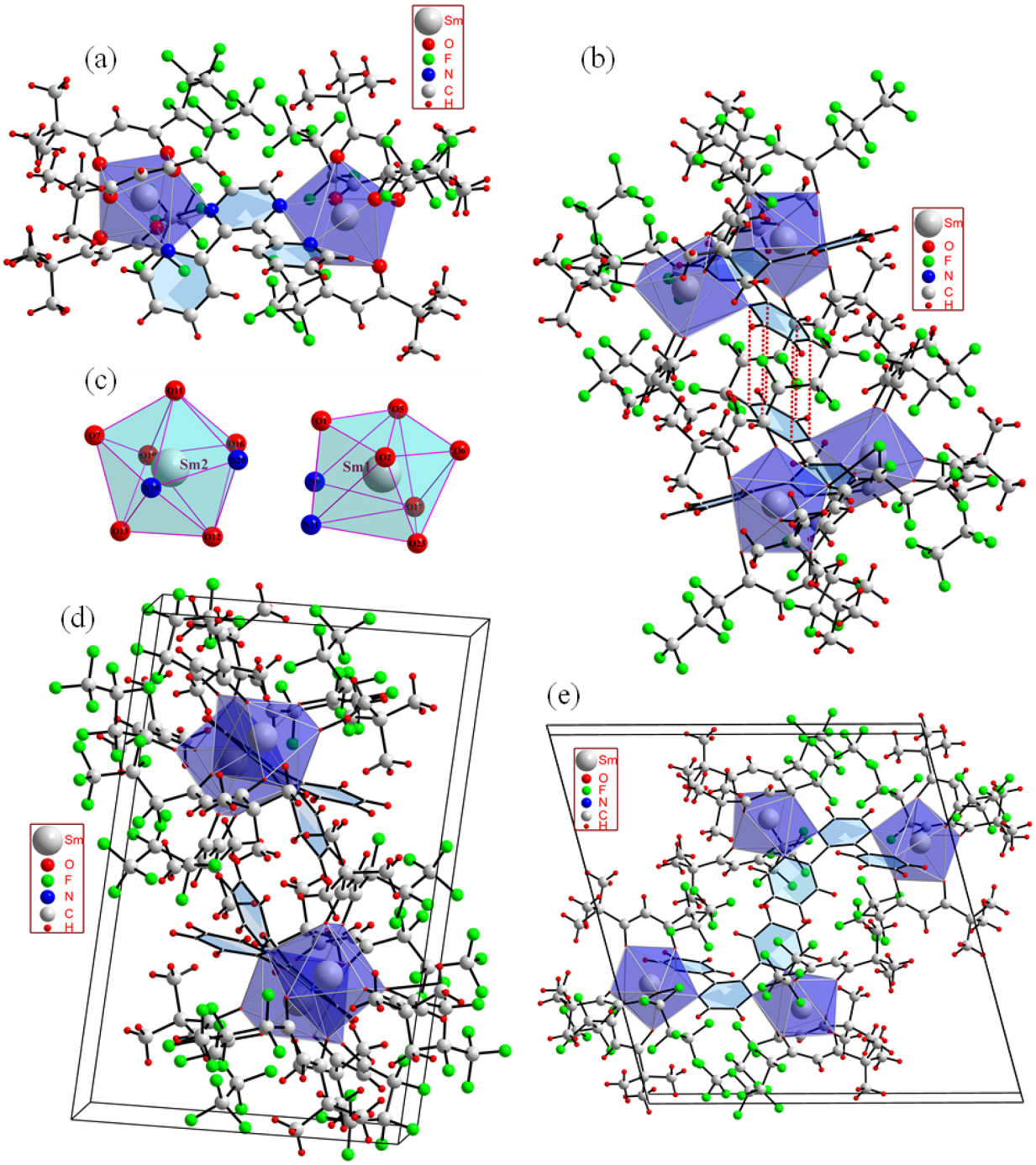

Figure 1. (a) Molecular structure of $[Sm(fod)_3(\mu\text{-bpp})Sm(fod)_3]$, (b) $\pi-\pi$ stacking between two molecular units, (c) shapes of the polyhedra of coordination sphere around the two metal ions in $[Sm(fod)_3(\mu\text{-bpp})Sm(fod)_3]$, and (d, e) the unit cell views of the complex from two perpendicular directions.

Eu). The longer Sm−Sm intermetallic distance can also be related to the larger size of Sm^{3+}. The Eu−N bond lengths and Eu−Eu intermetallic distance for the present complex under study are shorter than those reported for the bpp bridged dinuclear complex $[Eu(tta)_3]_2(bpp)$ (tta = 4,4,4-trifluoro-1-(2-thienyl)-1,3-butanedione).[62] It could be due to the presence of perfluoryl group in the fod moiety, which increases the residual acidity of europium, making it a better complexing site for the incoming donors. Therefore, the europium ions attract the bpp more strongly, resulting in shorter Eu−Eu and Eu−N distances. However, the Eu−O (2.35 Å) and Eu−N (2.62 Å) bond distances for the $[Eu(fod)_3(\mu\text{-bpp})Eu(fod)_3]$ complex are longer than the Eu−O (2.33 Å) and Eu−N (2.57 Å) bond distances reported for mononuclear $[Eu(tdh)_3(bpp)]$[63] (tdh is 1,1,1-trifluoro-5,5-dimethyl-2,4-hexanedione). Both Sm^{3+} and Eu^{3+} complexes are stabilized by the $\pi-\pi$ stacking interactions between the two pyridine rings of bpp with interplanar distances of 4.11 Å (Figures 1b and 2b). Similar interplanar $\pi-\pi$ interactions are also reported between the rings of indazole in the complexes $[Eu(hfaa)_3(indazole)_3]$ and $[Dy(hfaa)_3(indazole)_2]$.[22] The torsion angle of two pyridine rings with respect to the pyrazine ring has been reported to be 5.4°

https://doi.org/10.1021/acsomega.0c05976
ACS Omega 2021, 6, 21207−21226

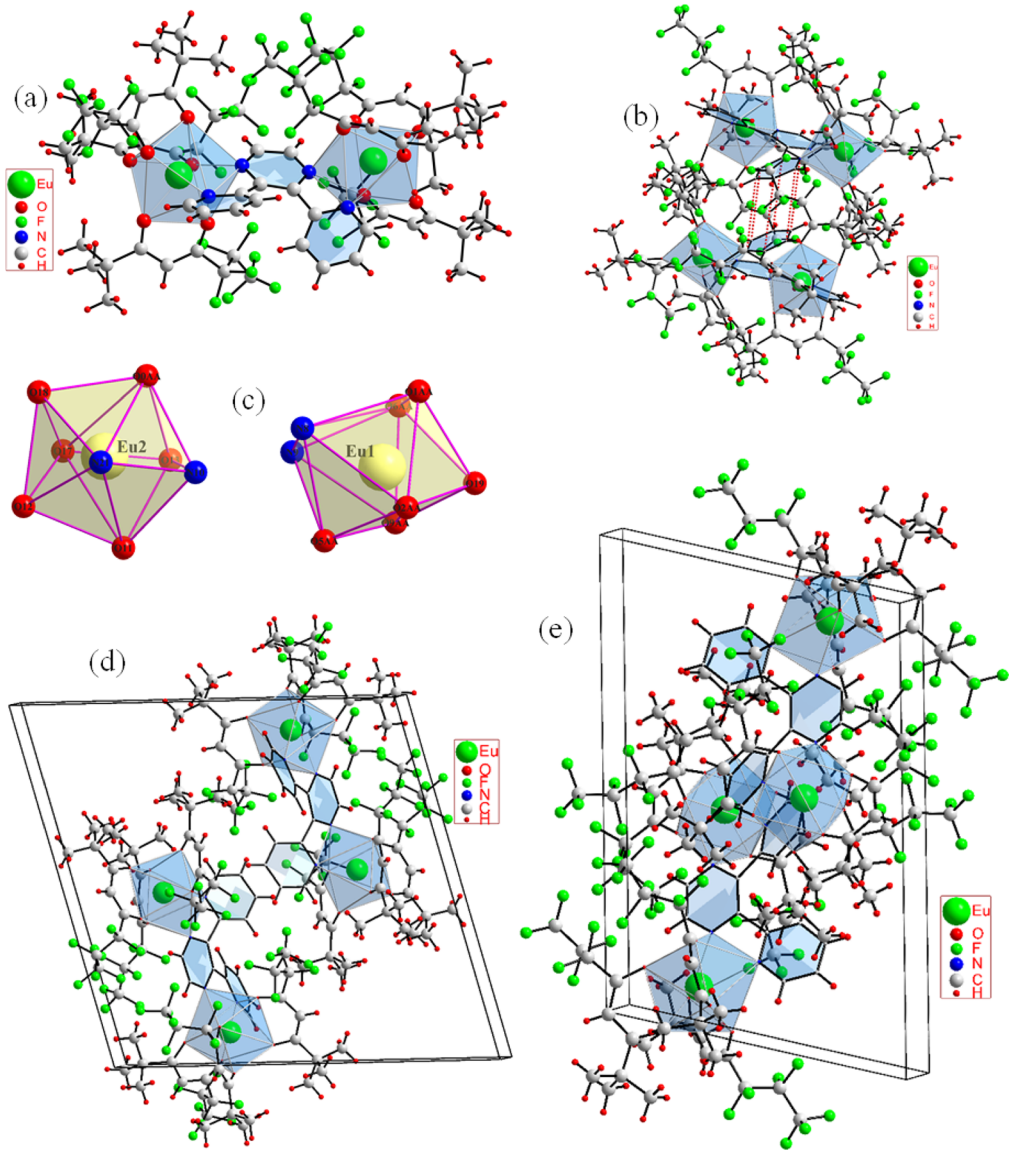

Figure 2. (a) Molecular structure of $[Eu(fod)_3(\mu\text{-bpp})Eu(fod)_3]$, (b) $\pi-\pi$ stacking between two molecular units, (c) shapes of the polyhedra of coordination sphere around the two metal ions in $[Eu(fod)_3(\mu\text{-bpp})Eu(fod)_3]$, and (d, e) the unit cell views of the complex from two perpendicular directions.

in the crystal structure of free bpp.[64] However, this angle is 17.9° (C10−C3−C4−C5) in the Sm^{3+} complex and 19.1° (C10−C3−C4−C5) in the Eu^{3+} complex. In addition to the torsion induced into the bpp upon coordination with the $Ln(fod)_3$ moieties (Ln = Sm^{3+} and Eu^{3+}), the pyrazine ring is also more deviated from its planarity than it had in the free bpp.[64]

The optimized structure of the complexes was obtained using Sparkle RM1 and PM7 (Figures S1−S4). The average bond lengths predicted by Sparkle RM1 and PM7 for metal to oxygen and metal to nitrogen are in close agreement to the results found from the crystal structure analysis for the complexes (Table 3). The Sparkle RM1 and PM7 optimized structures of the Eu^{3+} complex show the root mean square deviation (RMSD) of 2.217 and 2.878 Å, respectively, from the crystal structure. Similarly, the RMS deviation of Sparkle RM1 and PM7 optimized structures from the crystal structure of the Sm^{3+} complex is 2.675 and 2.564 Å, respectively. In both cases, the RMS deviation values are lower than those reported for the Sparkle/RM1 optimized structure of the tetra-europium centered molecule (5.07 Å) with respect to its crystal structure.[36] The lower RMSD values for the optimized structures indicate the accuracy of the Sparkle RM1 and PM7 in predicting the structures of the complex structures.

2.2. Shape Analysis. The shape analysis was performed using the reported method by Haigh.[65] For the eight-coordinate metal centers, the most encountered shapes are square antiprism (SAP), bicapped trigonal prism (BCTP), and dodecahedron (D). These shapes have 16, 17, and 18 edges, respectively. The two adjacent atoms depicting an edge subtend an angle at the central metal atom (Figure S5). Therefore, there are 16, 17, and 18 angles, respectively, subtended by the 16, 17, and 18 edges of square antiprism, bicapped trigonal prism, and dodecahedron shapes at the central metal atom. The total number of angles in an eight-coordinate polyhedron subtended at the central metal atom by all the possible pairs of the coordinated 8 ligand atoms is 28 (including both adjacent and non-adjacent pair of atoms). For

https://doi.org/10.1021/acsomega.0c05976
ACS Omega 2021, 6, 21207−21226

Table 2. Bond Lengths between Metal Ions and Atoms around the Coordination Sphere of the Complexes

$[Sm(fod)_3(\mu\text{-bpp})Sm(fod)_3]$		$[Eu(fod)_3(\mu\text{-bpp})Eu(fod)_3]$	
Sm1−O7	2.403	Eu1−O7	2.331
Sm1−O8	2.379	Eu1−O8	2.358
Sm1−O9	2.403	Eu1−O9	2.371
Sm1−O10	2.377	Eu1−O10	2.319
Sm1−O11	2.405	Eu1−O11	2.350
Sm1−O12	2.355	Eu1−O12	2.374
Sm1−N3	2.625	Eu1−N1	2.594
Sm1−N4	2.626	Eu1−N2	2.593
Sm2−N1	2.688	Eu2−N3	2.656
Sm2−N2	2.650	Eu2−N4	2.622
Sm2−O1	2.348	Eu2−O1	2.332
Sm2−O2	2.407	Eu2−O2	2.350
Sm2−O3	2.385	Eu2−O3	2.396
Sm2−O4	2.376	Eu2−O4	2.336
Sm2−O5	2.358	Eu2−O5	2.346
Sm2−O6	2.368	Eu2−O6	2.358

the shapes (vide supra), the angles subtended by the edges at the central metal atom must be the smallest of the total number (28) of angles and the change between the two consecutive angles among them must be very small. Therefore, for square antiprism 16, for bicapped trigonal prism 17, and for dodecahedron 18, angles must be the smallest of the total 28 angles in ascending order. All the possible 28 angles of the individual polyhedron of the complexes of Sm^{3+} and Eu^{3+} in the ascending order are presented in Tables S1 and S2. In the case of the Sm1 center of the Sm^{3+} complex and Eu1 center of the Eu^{3+} complex, the 17th angle abruptly increases compared to the smaller 16th angle (Tables S1 and S2). The difference between the 16th and the 17th angle is 21.1° (Sm1 center of the Sm^{3+} complex) and 20.4° (Eu1 center of the Eu^{3+} complex). These values suggest that the arrangement of the ligands around the two centers is square antiprismatic[65] (Figures 1c and 2c). In the case of the second samarium center Sm2 of the Sm^{3+} complex, the difference between the 16th and 17th lowest angle is 11.7° and the difference between the 17th and 18th smallest angle is 12.9° (Table S1). Similarly, in the case of the Eu^{3+} complex, these values for the second europium center Eu2 are 11.4 and 11.6°, respectively (Table S2). These values suggest that the arrangement of the ligands around Sm2 and Eu2 is neither square antiprismatic nor dodecahedron, rather an arrangement between the two geometries, which are more inclined toward a dodecahedron arrangement[65] (Figures 1c and 2c).

The results obtained using the method reported by Chen[86] were further authenticated by computing the distortions of the coordination polyhedra from the ideal eight-coordinate geometries using SHAPE software.[66] The results are presented in Tables S3 and S4. The SHAPE software[66] calculates the deviation for a given polyhedron from an ideal eight-coordinate polyhedron (square antiprism, bicapped trigonal prism, and dodecahedron, etc.), and the one with the least deviation is accepted. The least deviation has been found for the square antiprism (D_{4d}) geometry in the case of the coordination polyhedra around Sm1 and Eu1. Similarly, the smallest deviation has been found for the triangular dodecahedron (D_{2d}) geometry around Sm2 and Eu2 centers. These results obtained from SHAPE software[66] demonstrate that the results obtained using the method reported by Haigh[65] in the first place are correct and the method can be successfully used to assign shapes to the coordination polyhedra.

The results of the shape analyses of the coordination polyhedra of the Sparkle PM7 optimized structures reveal that the geometry around the two metal centers in a given Sm^{3+} and Eu^{3+} complex is similar to those obtained from the single-crystal X-ray analyses. That is, the shape of the polyhedra around the two unique metal centers in a given complex is not similar, with one metal center having a square antiprismatic arrangement of ligand atoms around it while the other center has a triangular dodecahedron geometry (Figures S6 and S7). However, the Sparkle RM1optimized structures show that, in the case of the Eu^{3+} complex, the shape around both Eu^{3+} centers is square antiprismatic while the shape around the two Sm^{3+} centers is triangular dodecahedron in the case of the Sm^{3+} complex (Figures S8 and S9). It is not in the agreement with the experimental results obtained from the single-crystal analysis. Therefore, it is concluded that the Sparkle RM1 does not work satisfactorily for the complexes investigated here. The distortions calculated from the ideal eight-coordinate geometries using SHAPE software[66] for Sparkle PM7 and RM1 are presented in Tables S5−S8.

2.3. ^{1}H NMR Spectra. The one-dimensional (^{1}H NMR) and two-dimensional (^{1}H-^{1}H COSY) spectra were used to assign the NMR signals of the bpp and the complexes. The chemical shifts of the free ligand and the complexes are presented in Table 4. The ^{1}H NMR spectra (1D and COSY correlation) of the free ligand 2,3-bis(2-pyridyl)pyrazine (bpp) exhibit four resonances at 8.68, 8.36, 7.76, and 7.21 ppm (δ) in the intensity ratio of 1:1:2:1 (Figures S10 and S11). The pyrazine ring protons (H-1) resonate as a singlet at 8.68 ppm (δ). The other three signals are due to the protons of the pyridine rings. The H-2 protons that are nearer to pyridyl nitrogen appear at 8.38 ppm (δ) as a doublet. The H-4 and H-5 protons appear as a combined multiplet at 7.76 ppm (δ), and the H-3 protons resonate as an asymmetric triplet at 7.21 ppm (δ). The proton resonances of free bpp assigned by ^{1}H-^{1}H COSY conform with the report available in the litreature.[52] The NMR spectra of the complexes are consistent with the presence of coordinated bpp. The NMR spectra of the diamagnetic complexes $[La(fod)_3(bpp)]$ (Figure S12) and $[Lu(fod)_3(\mu\text{-bpp})Lu(fod)_3]$ (Figures 3 and 4) show four signals for the coordinated bpp and one resonance each for methine and *t*-butyl group of the β-diketone. The methine and

Table 3. Average Bond Lengths

	Sm1−O	Sm1−N	Sm2−O	Sm2−N	Eu1−O	Eu1−N	Eu2−O	Eu2−N
crystal structure	2.387	2.625	2.374	2.669	2.351	2.594	2.353	2.639
sparkle/RM1	2.412	2.587	2.414	2.588	2.388	2.519	2.385	2.522
sparkle/PM7	2.382	2.559	2.380	2.561	2.382	2.559	2.382	2.555

https://doi.org/10.1021/acsomega.0c05976
ACS Omega 2021, 6, 21207−21226

Table 4. Chemical Shifts[a] and Paramagnetic Shifts[b] of the Complexes

	H-1	H-2	H-3	H-4	H-5	CH	Bu^t
bpp	8.68(s)	8.38(d)	7.21(t)	7.76(m)	7.76(m)		
[La(fod)$_3$(bpp)]	8.99(s)	8.86	7.40(m)	7.70(t)	7.39(m)	5.88	1.05
[Lu(fod)$_3$(μ-bpp)Lu(fod)$_3$]	9.32	9.25	7.49	7.67	7.47	5.87	1.06
[Sm(fod)$_3$(μ-bpp)Sm(fod)$_3$]	7.16 (−2.16)	6.23(d) (−3.02)	7.21(t) (−0.28)	7.04 (−0.63)	8.11 (0.64)	7.04 (1.17)	1.01 (−0.05)
[Eu(fod)$_3$(μ-bpp)Eu(fod)$_3$]	16.98 (7.61)	17.72 (8.47)	15.14 (7.44)	11.78 (4.39)	10.23 (2.84)	2.59 (−3.29)	1.41 (0.36)

[a]Chemical shifts are presented in parts per million (ppm) relative to the internal standard tetramethylsilane (TMS). Positive and negative chemical shifts are plotted downfield and upfield, respectively. [b]The paramagnetic shift, given in parentheses, is the difference between chemical shifts of a given proton in the paramagnetic complex and diamagnetic Lu complex.

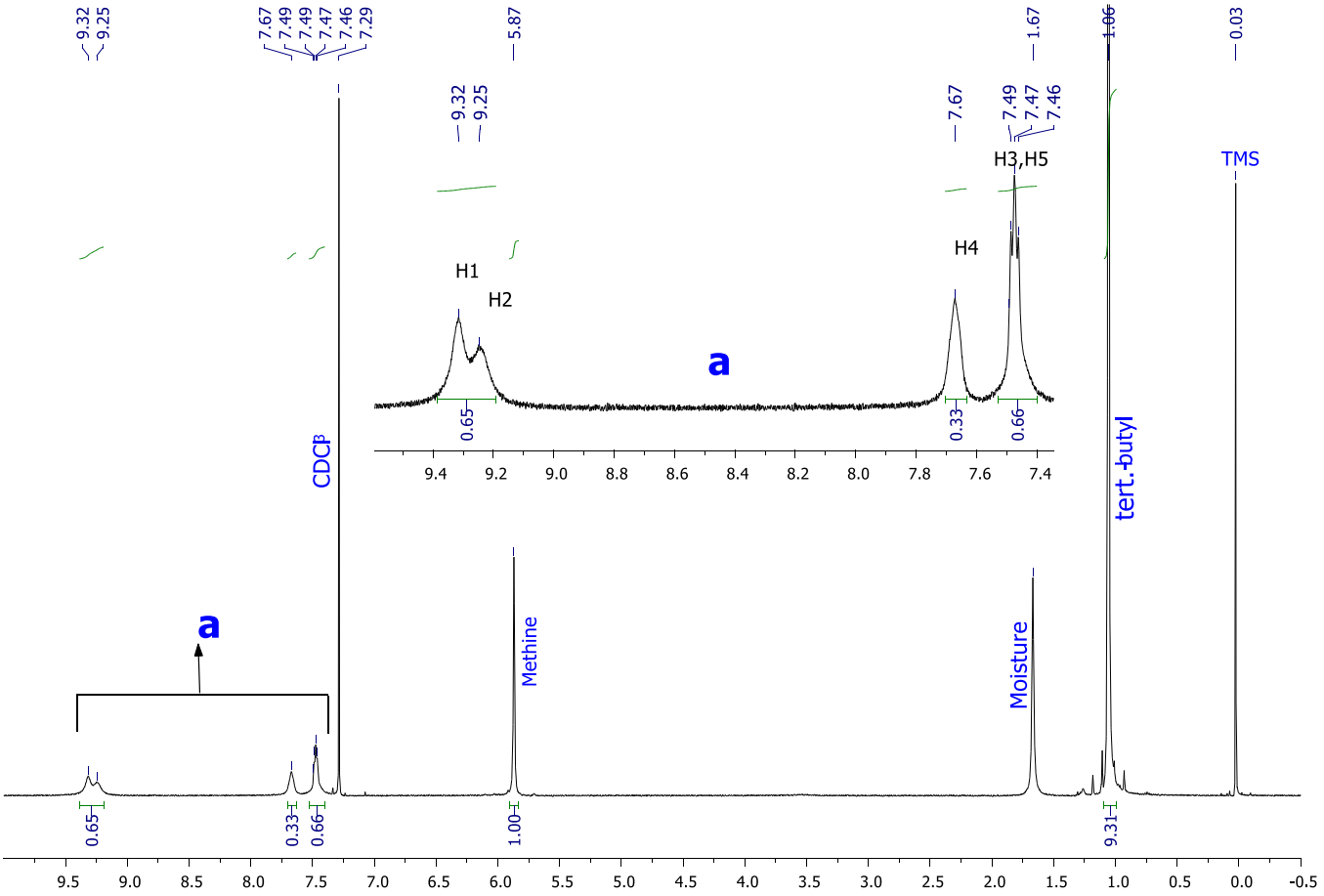

Figure 3. 500 MHz ^{1}H NMR spectra at 298 K of [Lu(fod)$_3$(μ-bpp)Lu(fod)$_3$], (a) enlarged portion from 7.2 to 9.7 ppm of spectra.

t-butyl resonances appear in a 1:9 intensity ratio. The magnitude of the inductive effect of coordination[67] in the case of the Lu^{3+} complex is stronger and is manifested by the larger downfield shifts of H-1 and H-2 protons, which are closer to the Lu^{3+}.

The NMR spectra of the paramagnetic complexes are more interesting where the bpp signals are shifted to higher fields (in the case of the Sm^{3+} complex) as well as to the lower fields (in the case of the Eu^{3+} complex). The NMR spectra of the Sm^{3+} complex display six resonances in the intensity ratio of 1:1:1:4:1:27, which have been assigned by 2D ^{1}H-^{1}H COSY NMR (Figures 5 and 6). Similarly, the NMR spectra of the Eu^{3+} complex display six resonances in the intensity ratio of 2:1:1:1:3:27 (Figures S13 and S14). In both the paramagnetic complexes, the largest shift is noted for H-2 followed by H-1 protons, supporting the view that the bpp is acting as the bridge between the Ln(fod)$_3$ units through the nitrogen atoms of pyrazine and pyridine rings. In the case of [Sm(fod)$_3$(μ-bpp)Sm(fod)$_3$], the methine resonance coalesce with the H-4 proton signal of bpp and appears at 7.04 ppm. The other signals due to bpp protons, except H-5, are shifted to up fields with H-2 showing the highest shift followed by and H-1 due to their proximity to the metal ion. In the Eu^{3+} complex, all resonances of coordinated bpp are shifted to down fields with the largest downfield shift for H-2 followed by H-1. Meanwhile, the methine proton signal has moved to the upfield side. The *t*-butyl could not be shifted to the higher field side, instead has been de-shielded and appears at the lower field. Such exceptions are available in the litreature.[67] This result and reports available in the literature[68,69] suggest that the induced paramagnetic shifts are dipolar in nature. The NMR spectra of the complexes show no resonance for free bpp or free β-diketone; no change in signal line width or position is noted even on keeping the solutions for a few days.

2.4. UV/Visible Absorption Spectra. The absorption spectra of the 10^{-5} M solution of free ligands and Sm and Eu

https://doi.org/10.1021/acsomega.0c05976
ACS Omega 2021, 6, 21207−21226

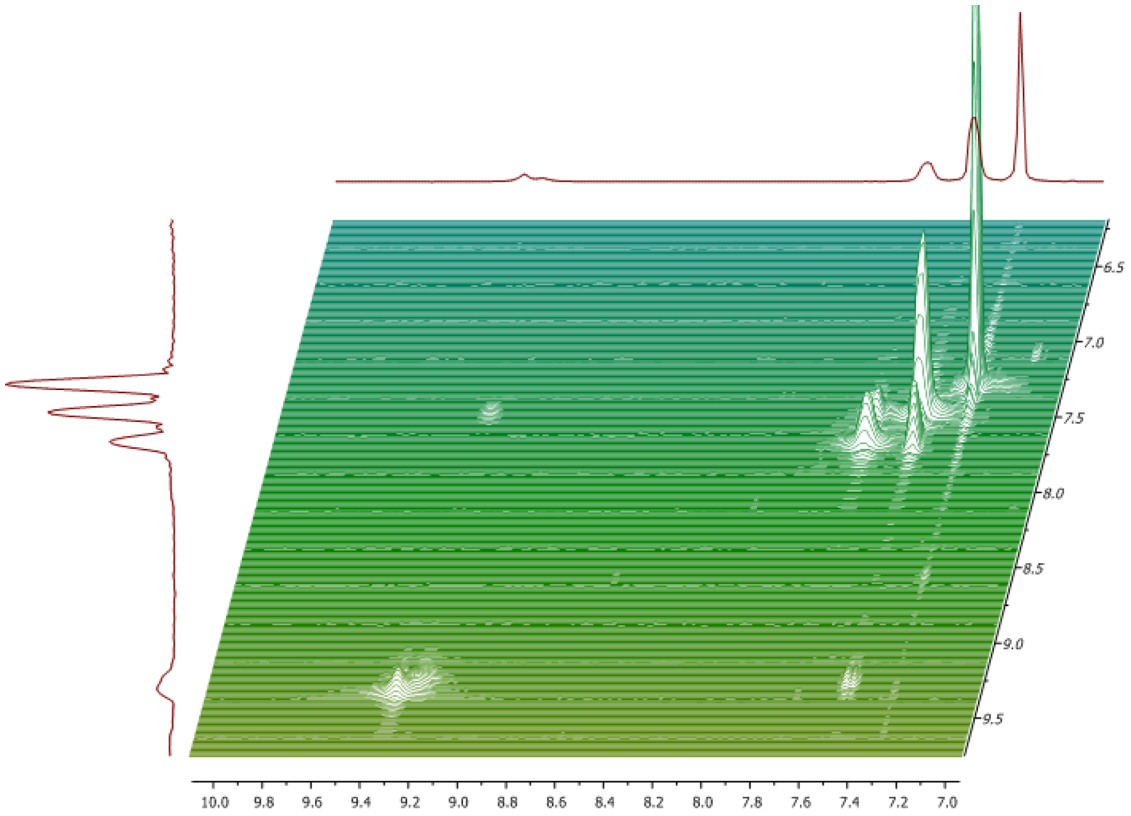

Figure 4. 500 MHz ^{1}H-^{1}H COSY spectra at 298 K of [Lu(fod)$_3$(μ-bpp)Lu(fod)$_3$].

complexes are presented in Figure 7. The free ligands absorb in the range of 240−330 nm, and the maxima (λ_{max}) appear at 296 nm (Hfod) and 286 nm (bpp). The absorption band of the ligands are shifted in the complexes and appear as a single band in the range of 240−380 nm with the maxima (λ_{max}) appearing at 293 nm. This band in the complexes is assigned to the $S_0 \rightarrow S_1$ ($\pi \rightarrow \pi^*$) transition. The shift of the band is due to coordination of the ligands to the metal ion. The molar extinction coefficients of [Sm(fod)$_3$(μ-bpp)Sm(fod)$_3$] (1.10×10^4 L mol^{-1} cm^{-1}) and [Eu(fod)$_3$(μ-bpp)Eu(fod)$_3$] (2.63×10^4 L mol^{-1} cm^{-1}) are higher than those of Hfod (8.10×10^3 L mol^{-1} cm^{-1}) and bpp (3.95×10^3 L mol^{-1} cm^{-1}). The increase in the molar extinction coefficient of the complexes than the ligands provides strong evidence that the Hfod and bpp have coordinated to the metal ions. The spectra of the [Sm(fod)$_3$(μ-bpp)Sm(fod)$_3$] and [Eu(fod)$_3$(μ-bpp)Eu(fod)$_3$] complexes were also obtained from 10^{-3} M chloroform solutions (Figure S15) in order to observe metal-based absorptions (4f-4f absorption are parity forbidden, therefore have very low absorptivity coefficients). It is noteworthy that the 4f-4f transitions appearing in the absorption spectra are also present in the excitation spectra of the complexes.

2.5. Luminescence. The luminescence spectra in the visible region are investigated in the solid state, solution (chloroform, dichloromethane, ethanol, and acetone), and PMMA polymer thin films. The emission spectra with the most intense emission peaks for the Sm^{3+} and Eu^{3+} complexes were obtained by recording the emission spectra of the chloroform solutions at different excitation wavelengths (Figures S16 and S17). The excitation spectra are obtained by monitoring the most intense emission peak of the complexes. These are at 642 nm ($^4G_{5/2} \rightarrow {}^6H_{9/2}$) for the Sm^{3+} complex and 614 nm ($^5D_0 \rightarrow F_{7/2}$) for the Eu^{3+} complex. The excitation spectra of the complexes in different solvents (Figure 8) appear in the range of 325−430 nm with maxima (λ_{max}) at 351 nm (acetone), 363 nm (chloroform), 359 nm (dichloromethane), and 361 nm (ethanol) for the Sm^{3+} complex and 358 nm (acetone), 364 nm (chloroform), 361 nm (dichloromethane), and 361 nm (ethanol) for the Eu^{3+} complex. These are $\pi-\pi^*$ transitions ($S_0 \rightarrow S_1$) of the organic ligands (fod and bpp). The maximum wavelength (λ_{max}) was used to obtain the emission spectra in the respective solvents. The excitation bands in the case of solid complexes are more intense and much broader than those observed for the solution (Figures 8 and 9). The excitation bands for the solid complexes extend up to 440 nm with maxima at 354 nm (Sm^{3+} complex) and 261 nm (Eu^{3+} complex). The excitation spectra of the thin films (Figures S18 and S19) show broad bands in the range of 230−360 nm (for the Eu^{3+} complex) and 330−390 nm (for the Sm^{3+} complex). The excitation spectra of thin films broaden and show red shift on increasing the concentration of complexes in the PMMA polymer. These results corroborate with those reported for [Eu(fod)$_3$(H$_2$O)$_2$]-doped PMMA films.[70] The excitation spectra mimic the absorption spectra, suggesting that the energy is absorbed through the $\pi-\pi^*$ transitions ($S_0 \rightarrow S_1$) of the organic ligands (fod and bpp) and then transferred to the metal ion.

The emission spectra of the samarium complex display three characteristic emission peaks $^4G_{5/2} \rightarrow {}^6H_{5/2}$ (561 nm), $^4G_{5/2} \rightarrow {}^6H_{7/2}$ (596 nm), and $^4G_{5/2} \rightarrow {}^6H_{9/2}$ (642 nm) in each solvent and hybrid thin films (Figure 11 and Figure S20). The emission spectrum of the solid complex (Figure 10) displays an additional peak at 561 nm $^4G_{5/2} \rightarrow {}^6H_{11/2}$.[71,72] The electric-dipole transition $^4G_{5/2} \rightarrow {}^6H_{9/2}$ is the most intense, followed by $^4G_{5/2} \rightarrow {}^6H_{7/2}$ (magnetic-dipole) and $^4G_{5/2} \rightarrow {}^6H_{5/2}$ transitions. This indicates that the samarium complex lacks

https://doi.org/10.1021/acsomega.0c05976
ACS Omega 2021, 6, 21207−21226

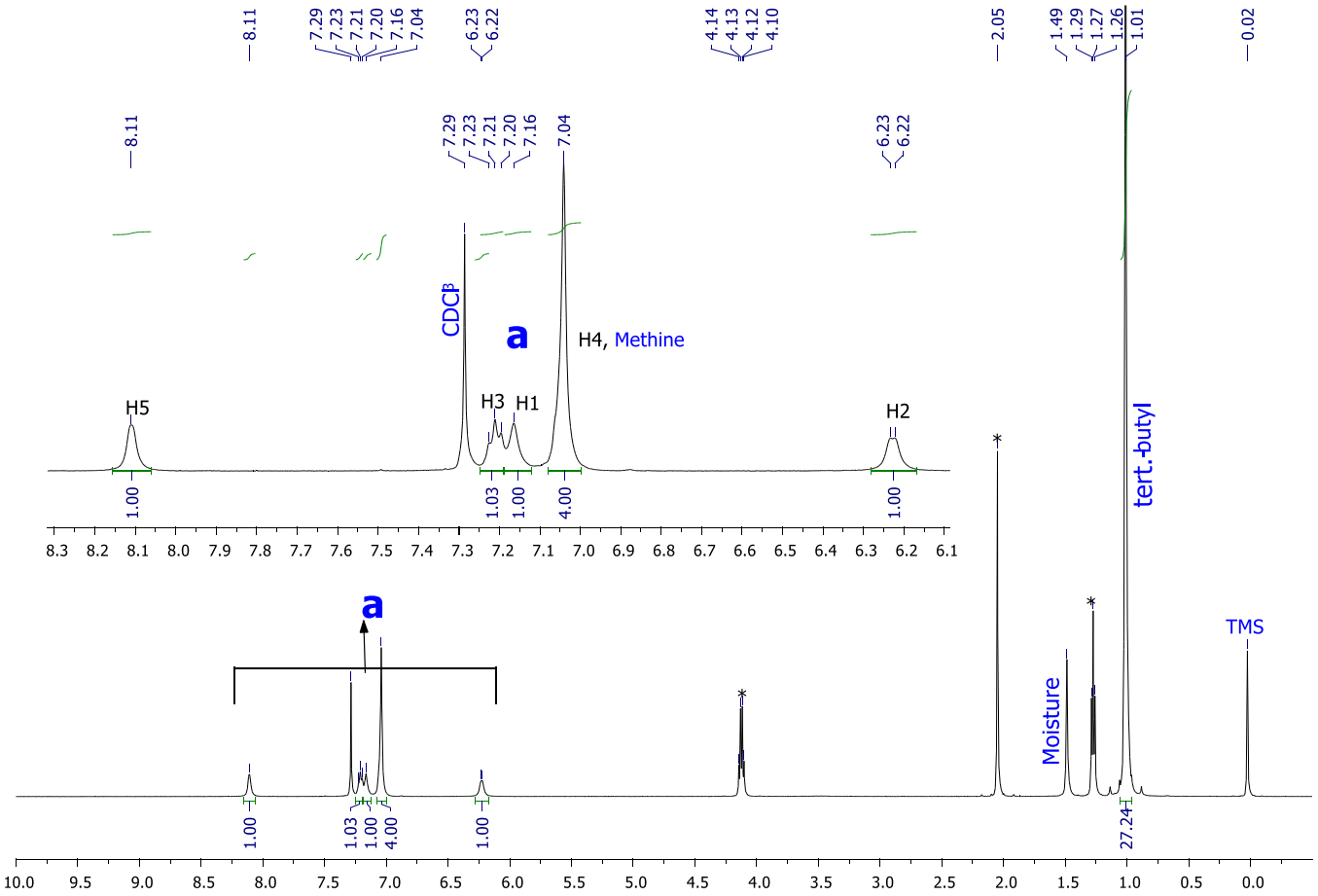

Figure 5. 500 MHz ^{1}H NMR spectra at 298 K of $[Sm(fod)_3(\mu\text{-bpp})Sm(fod)_3]$, (a) enlarged portion from 6.1 to 8.3 ppm of spectra.

an inversion center. It is reported that the intensity of the magnetic-dipole transition ($^4G_{5/2} \rightarrow {}^6H_{7/2}$) is higher than the electric-dipole transition in centrosymmetric complexes.[73] Furthermore, the $^4G_{5/2} \rightarrow {}^6H_{7/2}$ transition shows stark splitting. The higher intensity of the electric-dipole transition and stark splitting in the magnetic-dipole transition are indicative of the fact that the complex has a distorted geometry, which results in higher asymmetry of the field around samarium. This corroborates with the results obtained from the shape analysis of the crystal structure. The coordination symmetry around the Sm^{3+} ion in a complex is determined by measuring the experimental energy parameter (η_{sm}), which represents the ratio of the integrated area under the peaks of $^4G_{5/2} \rightarrow {}^6H_{9/2}$ (electric-dipole) and $^4G_{5/2} \rightarrow {}^6H_{5/2}$ (magnetic-dipole) transition.[74] The η_{sm} of the solid complex and its solutions in different solvents are 8.71 (solid complex), 5.85 (chloroform), 4.92 (acetone), 4.6 (ethanol), and 4.31 (dichloromethane). It appears that the highest asymmetry of the field prevails in chloroform followed by acetone, ethanol, and dichloromethane. The highest asymmetry around the samarium is noted for the solid complex (η_{sm} = 8.71), which is evident from the very prominent stark splitting of the magnetic-dipole transition.

The emission spectra of the europium complex display five emission peaks, $^5D_0 \rightarrow {}^7F_0$ (578 nm), $^5D_0 \rightarrow {}^7F_1$ (590 nm), $^5D_0 \rightarrow {}^7F_2$ (614 nm), $^5D_0 \rightarrow {}^7F_3$ (651 nm), and $^5D_0 \rightarrow {}^7F_4$ (694 nm), in different solvents, the solid state, and thin films (Figures 10 and 11 and Figure S21). The electric-dipole transition $^5D_0 \rightarrow {}^7F_2$ transition is hypersensitive and is the most intense. The higher intensity of the $^5D_0 \rightarrow {}^7F_2$ transition is directly related to the asymmetry around the europium ion and higher polarizability of the ligands.[75] The bright red emission reflected in CIE coordinates of the europium complex is due to the highly intense $^5D_0 \rightarrow {}^7F_2$ transition. The intensity ratios (η_{Eu})[76] of $^5D_0 \rightarrow {}^7F_2/{}^5D_0 \rightarrow {}^7F_1$ transitions for the europium complex in acetone, chloroform, dichloromethane, and ethanol are 13.29, 12.80, 12.38, and 12.29, respectively. This intensity ratio (η_{Eu}) in the solid state is 11.54, and those in thin hybrid films are 11.67 (@5%(w/w)) and 12.28 (@10%(w/w)). The $^5D_0 \rightarrow {}^7F_2/{}^5D_0 \rightarrow {}^7F_1$ intensity ratio in all solvents, the solid state, and thin films is greater than that reported[77] for $[Eu(fod)_3(H_2O)_2]$ with η_{Eu} = 7.96, indicating that the intensity of $^5D_0 \rightarrow {}^7F_2$ has remarkably increased on complex formation with bpp. It reflects that bpp is a good sensitizer and effectively populates the emitting level of europium. The higher intensity ratio indicates that the ligand environment around the europium is highly polarized.[76] The Stark splitting of the $^5D_0 \rightarrow {}^7F_2$ transition is prominent in dichloromethane and in the solid state with three stark components. The band shape and stark components of the $^5D_0 \rightarrow {}^7F_2$ transition are typical of the fod complexes reported in the literature,[77−79] which could be due to the asymmetry of the tris fod Eu^{3+}complexes. The room temperature line width at half maximum (FWHM) of the $^5D_0 \rightarrow {}^7F_0$ transition in acetone, chloroform, dichloromethane, ethanol, the solid state, and in thin films @ 10%(w/w) and @5%(w/w) are 2.68, 2.21, 2.22, 2.28, 1.67, 1.51, and 1.52 nm, respectively (Figures S22 and S23). Only one line is observed for the non-degenerate

https://doi.org/10.1021/acsomega.0c05976
ACS Omega 2021, 6, 21207−21226

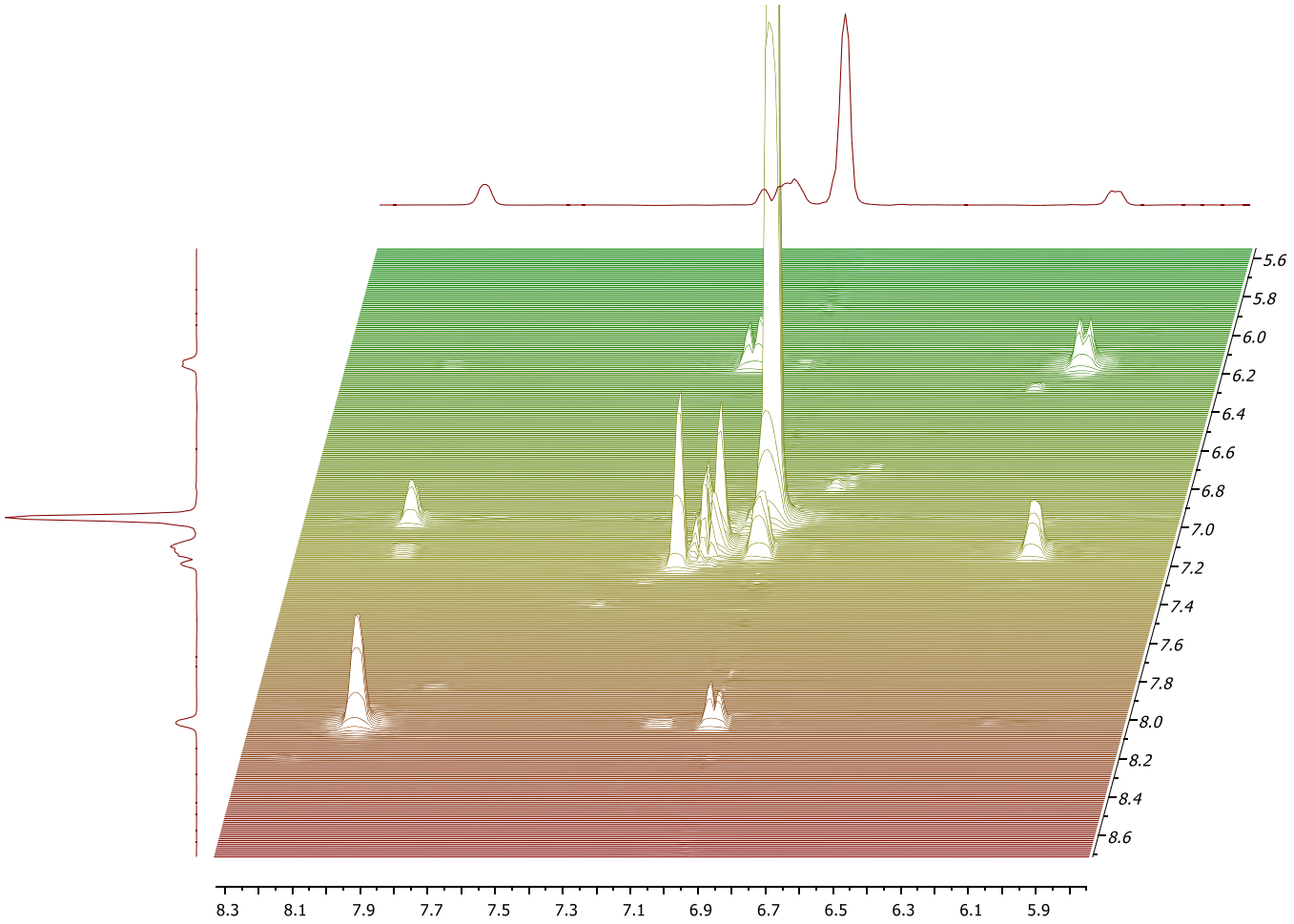

Figure 6. 500 MHz ^{1}H-^{1}H COSY NMR spectra at 298 K of [Sm(fod)$_3$(μ-bpp)Sm(fod)$_3$].

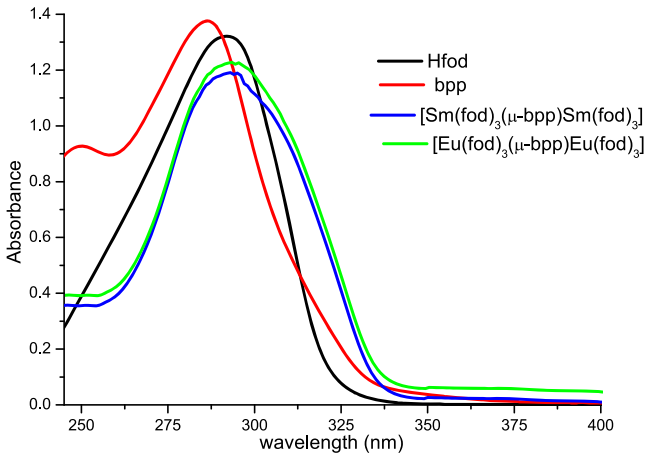

Figure 7. Absorption spectra of 10^{-5} M solutions of Hfod, bpp, [Sm(fod)$_3$(μ-bpp)Sm(fod)$_3$], and [Eu(fod)$_3$(μ-bpp)Eu(fod)$_3$] in chloroform.

$^{5}D_0 \rightarrow {}^{7}F_0$ transition, suggesting that only one type of Eu^{3+} species is emitting in the solution and the two Eu^{3+} sites are equivalent in the complex. This corroborates with the NMR results where only one set of signals is observed, suggesting that only one species is present in the solution. The presence of only one asymmetric shaped $^{5}D_0 \rightarrow {}^{7}F_0$ transition line in the solid state shows that the ligand symmetry around the two europium ions are similar with smaller structural difference.[80] The small width of FWHM of the $^{5}D_0 \rightarrow {}^{7}F_0$ transition indicates that the europium complex could be a potential material to be used in optoelectronic devices.[11,12] The splitting of the $^{5}D_0 \rightarrow {}^{7}F_1$ transition into two Stark components indicates that the environment around both the europium ions is asymmetric. It gets strong support from the results of shape analysis where both the Eu^{3+} centers have been found with distorted geometries (square antiprism and dodecahedron).

2.6. Decay Curves, Quantum Yield, and CIE Chromaticity. The decay curves at 300 K of the solutions, solid state, and thin films of both Sm^{3+} and Eu^{3+} complexes are fitted by a mono-exponential function (Figure 12 and Figures S24−S35). The mono-exponential functions indicate that there is only a single type of emitting centers in the complexes. It contrasts with the findings of the shape analysis, which predicts two distinct geometrical arrangements (square antiprism and dodecahedron) around the two metal centers in a given complex. There could be two reasons for the antithesis: (i) the emission and lifetime measuring instruments could not resolve the differences due their detecting limitations and (ii) the geometries of the two polyhedrons in a complex are not that dissimilar. The lifetime decay was monitored at 648 nm ($^{4}G_{5/2} \rightarrow {}^{5}H_{9/2}$) in the case of the Sm^{3+} complex and at 610 nm ($^{5}D_0 \rightarrow {}^{7}F_2$) in the case of the Eu^{3+} complex. The emission lifetimes of the $^{4}G_{5/2} \rightarrow {}^{5}H_{9/2}$ transition of the Sm^{3+} complex in different media are 28.58 μs (chloroform), 29.33 μs (dichloro-

https://doi.org/10.1021/acsomega.0c05976
ACS Omega 2021, 6, 21207−21226

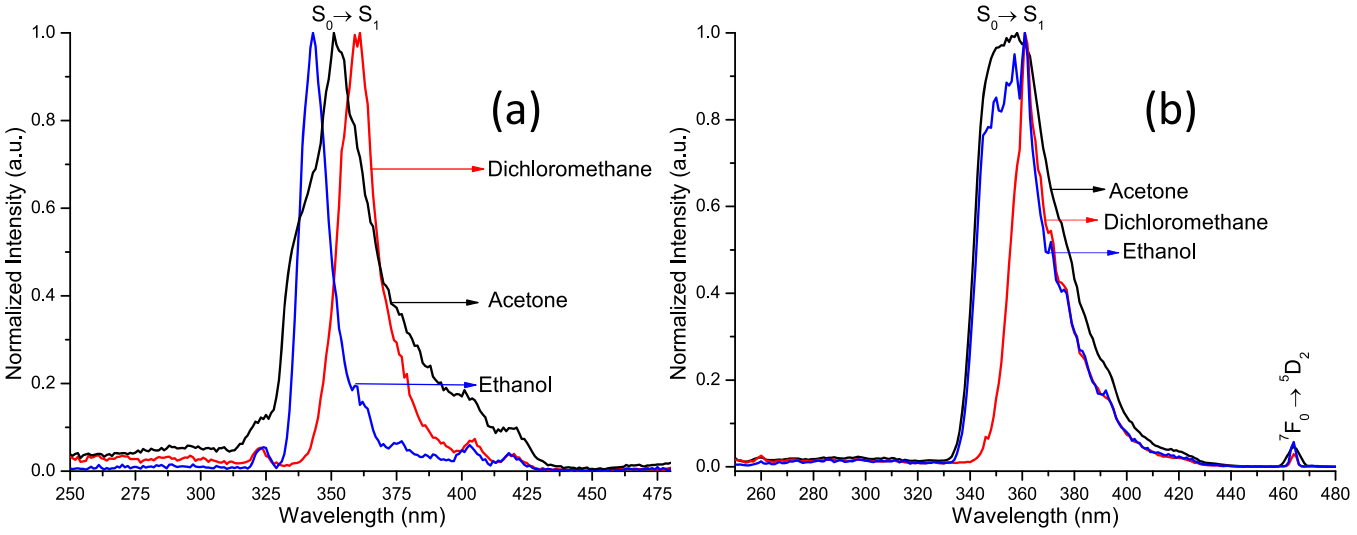

Figure 8. Excitation spectra of (a) [Sm(fod)$_3$(μ-bpp)Sm(fod)$_3$] and (b) [Eu(fod)$_3$(μ-bpp)Eu(fod)$_3$] in different solvents. Concentration = 5 × 10^{-5} M.

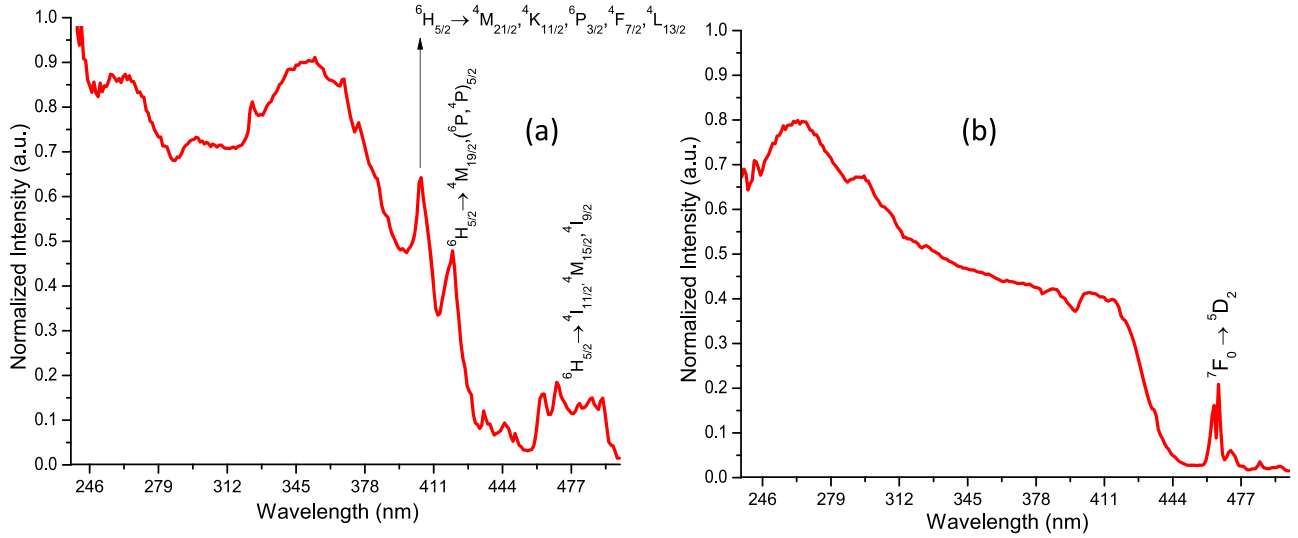

Figure 9. Solid-state excitation spectra of (a) [Sm(fod)$_3$(μ-bpp)Sm(fod)$_3$] and (b) [Eu(fod)$_3$(μ-bpp)Eu(fod)$_3$].

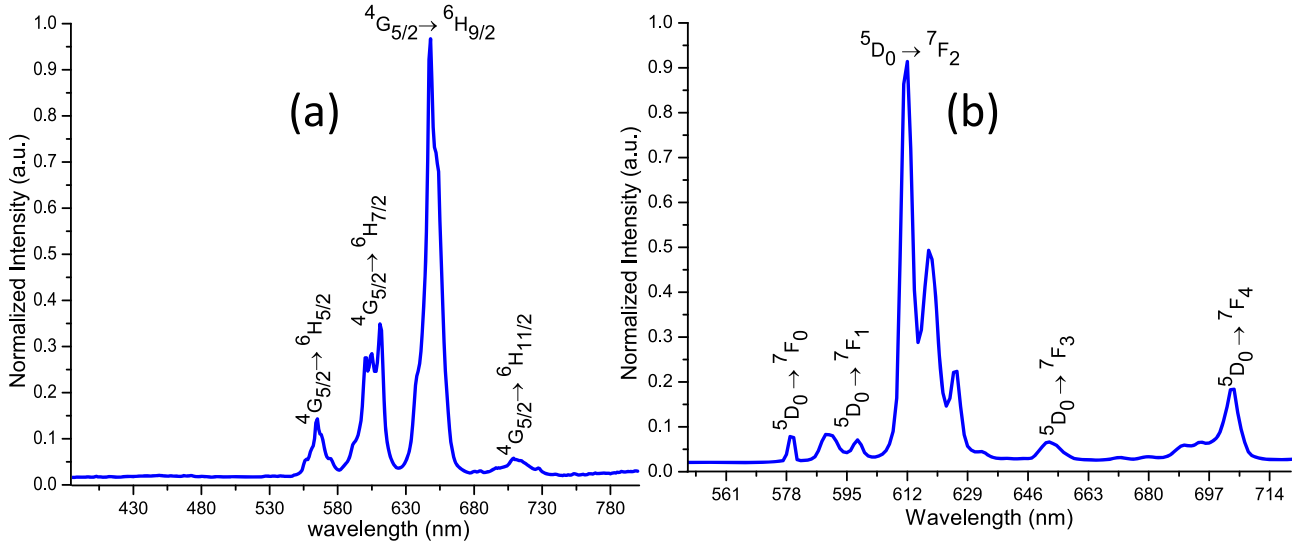

Figure 10. Emission spectra of (a) [Sm(fod)$_3$(μ-bpp)Sm(fod)$_3$] and (b) [Eu(fod)$_3$(μ-bpp)Eu(fod)$_3$] in the solid state.

https://doi.org/10.1021/acsomega.0c05976
ACS Omega 2021, 6, 21207−21226

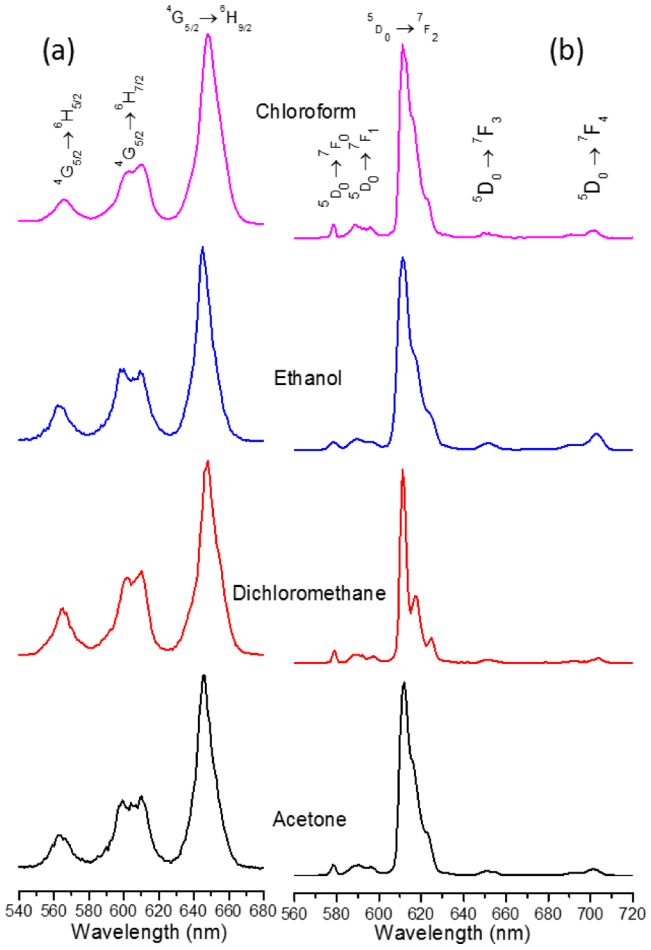

Figure 11. Emission spectra of (a) $[Sm(fod)_3(\mu\text{-bpp})Sm(fod)_3]$ and (b) $[Eu(fod)_3(\mu\text{-bpp})Eu(fod)_3]$ in different solvents. Concentration = 5×10^{-5} M.

methane), 25.97 μs (acetone), 21.58 μs (ethanol), and 38.74 μs (solid state). The higher lifetime in the solid state suggests that the impact of vibrational oscillators upon the decay of the excited state is lower in the solid state due to restricted degrees of freedom. The emission lifetime of the $^4G_{5/2} \rightarrow {}^5H_{9/2}$ transition for the Sm^{3+} complex in dichloromethane (29.33 μs) is greater than the lifetime of this transition reported for 2-thenoyltrifluoroacetonate (tta)-based complexes[81] in the same solvent. The lifetime of the $^5D_0 \rightarrow {}^7F_2$ transition in different media of the Eu^{3+} complex is 695.98 μs (chloroform), 584.34 μs (dichloromethane), 505.71 μs (acetone), 421.97 μs (ethanol), and 713.62 μs (solid state) (Table 5). The lifetime of the $^5D_0 \rightarrow {}^7F_2$ transition of the Eu^{3+} complex is much higher than bpp containing the mononuclear complex $[Eu(tdh)_3bpp]$ (300−414 μs) obtained in the temperature range of 323−273 K.[63] It is also higher than the lifetime of the same transition reported for $Eu(fod)_3$ (330 μs in chloroform and 620 μs in the solid state)[82] and $[Eu(fod)_3phen\text{-}NO]$.[83] The lifetimes of the $^5D_0 \rightarrow {}^7F_2$ transition of PMMA-doped films of $[Eu(fod)_3(\mu\text{-bpp})Eu(fod)_3]$ are 512.79 μs (10%(w/w)) and 520.30 μs (5%(w/w)). These are lower than that found for the solid

Table 5. Lifetime and Intrinsic Quantum Yield of Some Europium Complexes

complex	lifetime (ms)	Q_{Eu}^{Eu} %	reference
$[Eu(fod)_3(\mu\text{-bpp})Eu(fod)_3]$	0.71	56.99	present work
$[Eu(fod)_3H_2O]$	0.62	26.5	88
$[Eu(fod)_3phen]$	0.85	51	88
$[Eu(fod)_3(phen\ N\text{-}O)]$	0.37	43	84
$[P_{6,6,6,14}]^+[Eu(fod)_4]^-$	0.22	34	90
$[Eu(fod)_3tptz]$	0.71	54.30	24
$[Eu(fod)_3indazole]$	0.85	47.07	24
$[Eu(fod)_3impy]$	0.79	60.61	24
$[Eu(tta)_3(H_2O)_2]$	0.26	29	91
$[Eu(dbm)_3(H_2O)]$	0.06	3.44	92
$[Eu(dbm)_3(impy)]$	0.42	9.0	92
$[Eu(tfaa)_3(phen)]$	0.87	35.98	93
$[Eu(tfaa)_3(H_2O)]$	0.33	20.83	94
$[Eu(tfaa)_3(bpy)]$	0.87	31.56	95
$[Eu(hfaa)_3(impy)_2]$	0.98	32	96
$[Eu(hfaa)_3(pyz)_2]$	0.40	9.86	97

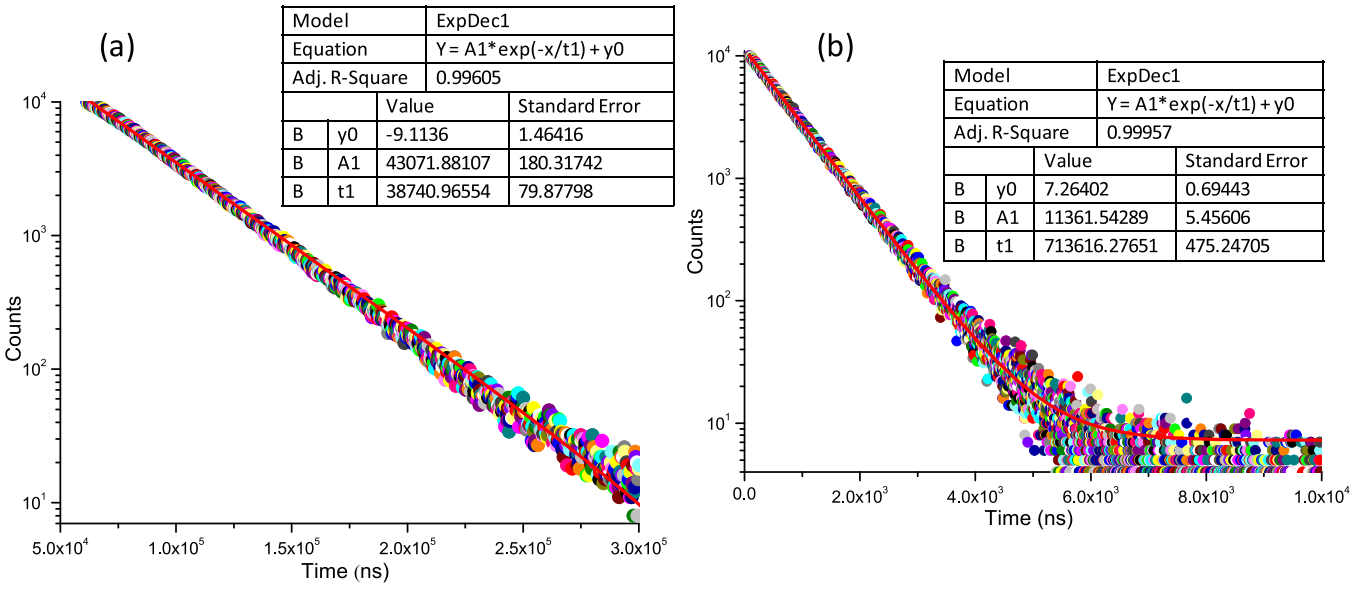

Figure 12. Emission decay curve of (a) $[Sm(fod)_3(\mu\text{-bpp})Sm(fod)_3]$ and (b) $[Eu(fod)_3(\mu\text{-bpp})Eu(fod)_3]$ in the solid state.

https://doi.org/10.1021/acsomega.0c05976
ACS Omega 2021, 6, 21207−21226

Table 6. CIE Chromaticity Coordinates (X_e, Y_e) in Different Phases for [Sm(fod)$_3$(μ-bpp)Sm(fod)$_3$] and [Eu(fod)$_3$(μ-bpp)Eu(fod)$_3$] Complexes

	CIE coordinates			CIE coordinates	
[Sm(fod)$_3$(μ-bpp)Sm(fod)$_3$]	X_e	Y_e	[Eu(fod)$_3$(μ-bpp)Eu(fod)$_3$]	X_e	Y_e
acetone	0.567	0.362	acetone	0.668	0.333
chloroform	0.621	0.388	chloroform	0.663	0.338
dichloromethane	0.581	0.377	dichloromethane	0.666	0.335
ethanol	0.540	0.351	ethanol	0.668	0.335
solid	0.607	0.370	solid	0.672	0.330
5%(w/w) PMMA	0.583	0.422	5%(w/w) PMMA	0.663	0.335
10%(w/w) PMMA	0.567	0.435	10%(w/w) PMMA	0.668	0.338

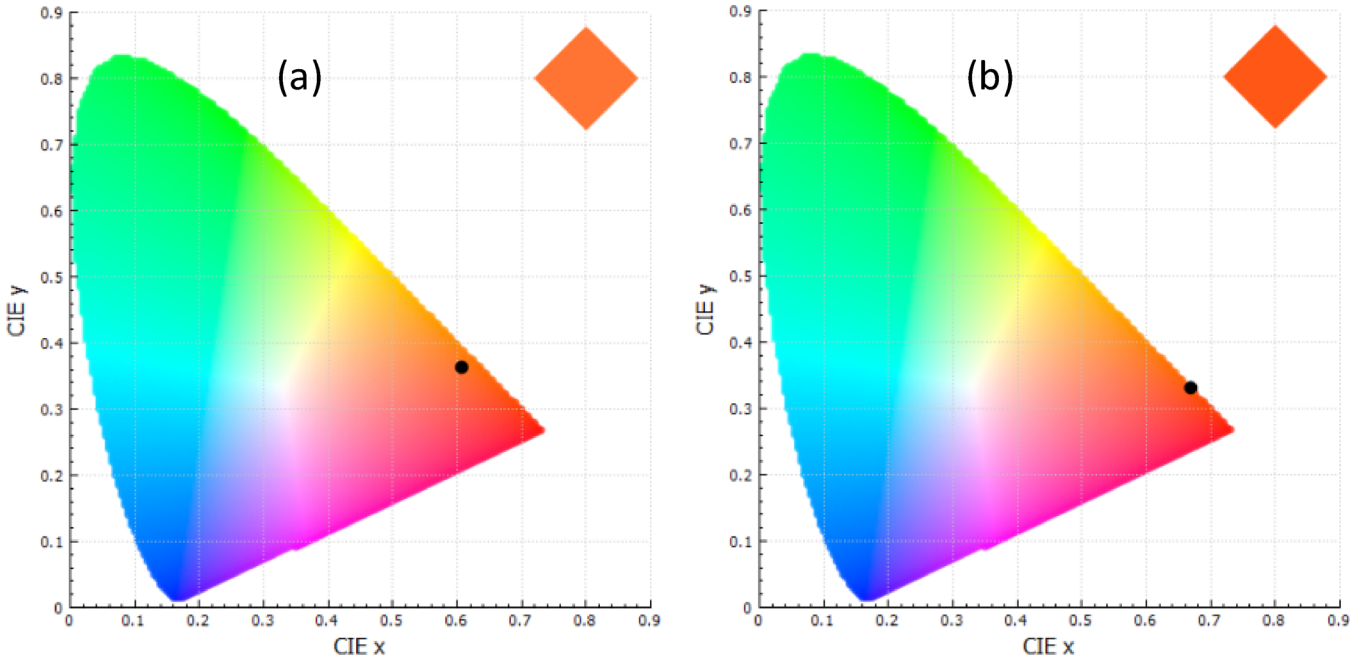

Figure 13. CIE chromaticity diagram of (a) [Sm(fod)$_3$(μ-bpp)Sm(fod)$_3$] and (b) [Eu(fod)$_3$(μ-bpp)Eu(fod)$_3$] in the solid state.

complex (713.62 μs), suggesting that the host polymer has a detrimental effect on the lifetime of the excited state. This is more pronounced in the case of PMMA-doped hybrid films of [Sm(fod)$_3$(μ-bpp)Sm(fod)$_3$] where the lifetime is much smaller for the polymeric films (6.73 μs 5%;w/w and 2.28 μs 10%;w/w) than the lifetime in the solid state. Similar results are reported for [Eu(fod)$_3$(H_2O)] where the lifetime in the PMMA film is smaller (440 μs) than the value in the solid state (620 μs).[70] It is interesting to note that, for both the complexes, the lifetime in non-coordinating solvents (chloroform and dichloromethane) are higher than those observed in coordinating solvents (acetone and ethanol). This could be related to (i) the presence of a large number of C−H oscillations in the coordinating solvents (acetone and ethanol), which depopulate the excited state of the Sm^{3+} and Eu^{3+} metals through high energy C−H and O−H vibrations and (ii) invasion of the coordination sphere. A similar result is reported for the Eu(fod)$_3$.[82]

The intrinsic quantum yield for the samarium complex is calculated using the equation $Q_{Sm}^{Sm} = \tau_{exprimental}/\tau_o$ ($\tau_{experimental}$ is the experimentally measured radiative lifetime and τ_o is the calculated average natural lifetime (3.25 ms) of Sm^{3+}.[84−87] The quantum yields calculated for the samarium complex in acetone, chloroform, dichloromethane, and ethanol are 0.80%, 0.88%, 0.90%, and 0.66%, respectively. The quantum yield, in the case of the solid state, is 1.19%, which is higher than those obtained from the solution. Similarly, for the Eu^{3+} complex, the quantum yield in the solid state is greater than those obtained from the solutions and thin hybrid films (Table 5). The higher intrinsic quantum yield of the complexes in the case of the solid state could be due to loss of energy of excited states through the dipole−dipole coupling interactions with the solvent or PMMA molecules.[81] The intrinsic quantum yield of the Eu^{3+} complex is much higher than its precursor [Eu(fod)$_3$$H_2O$] ($Q_{Eu}^{Eu}$ % = 26.5),[88] which indicates that the radiative emission from the excited state $^5D_0$ of the europium complex is very intense.

The CIE color coordinates of Sm^{3+} and Eu^{3+} complexes in solutions, the solid state, and thin films were calculated using LUMPAC software[89] (Table 6). The Sm^{3+} complex shows orange color emission with its color coordinates greatly influenced by the host medium (Figure 13a and Figure S36). The change in color coordinates can be due to the influence of ligand fluorescence on the overall spectra of the Sm^{3+} complex in different media. The europium complex shows red emission, and the color coordinates are nearly similar in all media (Figure 13b and Figure S37). The overall intensity of emission lines of the samarium ion is lower than the europium ion, which means that ligand fluorescence is influencing the CIE coordinates more in the case of the Sm^{3+} complex.

https://doi.org/10.1021/acsomega.0c05976
ACS Omega 2021, 6, 21207−21226

Table 7. Experimental Intensity Parameters of $[Eu(fod)_3(\mu\text{-bpp})Eu(fod)_3]$ in Different Solvents, Thin Films, and the Solid State

$[Eu(fod)_3(\mu\text{-bpp})Eu(fod)_3]$	Ω_2 (10^{-20} cm^2)	Ω_4 (10^{-20} cm^2)	Ω_2/Ω_4	τ_{obs} (μS)	τ_{rad} (μS)	A_{rad} (S^{-1})	A_{nrad} (S^{-1})	Q^{Eu}_{Eu}%
acetone	23.33	2.45	9.52	505.71	1714.74	583.18	1394.28	29.49
chloroform	22.35	5.51	4.06	695.67	1042.58	712.97	724.44	49.60
dichloromethane	21.66	2.11	10.12	584.34	1602.92	623.86	1087.59	36.45
ethanol	21.60	2.33	9.27	421.96	1831.13	546.11	1823.56	23.05
solid state	20.19	9.98	2.02	713.62	1252.08	798.67	602.68	56.99
TF10	21.45	2.77	7.74	512.79	1358.84	735.92	1214.16	37.74
TF5	20.39	3.07	6.64	520.30	1412.36	708.03	1213.94	36.84

2.7. Experimental and Theoretical Intensity Parameters. The electronic transitions within 4f subshells are strictly forbidden under parity law. However, the mixing of upper shell wave functions with 4f subshells under the influence of odd parameters of ligand field induces some even parity in 4f subshells. This results in states of mixed parity through which electric-dipole transitions can be forced to occur. These transitions are sharp with small band widths and are used as a source of laser. The intensity of magnetic-dipole transition is field-independent and can be calculated from the wave functions of free ions. However, for induced electric-dipole transitions, calculation of wave functions is difficult, and parameterization is necessary, which is provided in the Judd–Ofelt theory.[49,50]

The Judd–Ofelt intensity parameters (Ω_λ, λ = 2, 4, and 6) in the case of Eu can be deduced from the intensity of emission transitions. Since the absolute intensity of transitions could not be calculated, therefore, the intensity of the $^5D_0 \rightarrow {}^7F_1$ magnetic-dipole transition is used as a reference with dipole strength (D_{md}) of 9.6×10^{-42} esu^2 cm^2 and the parameters of other transitions are calculated relative to it.[98] The Ω_λ parameters are calculated using eq 1

$$\Omega_\lambda = \frac{D_{md}\nu_1^3}{e^2\nu_\lambda^3[\langle\psi J|U^\lambda|\psi J'\rangle]^2}\,\frac{9n^3}{\eta(\eta^2+2)^2}\,\frac{\int I_\lambda \nu\, d\nu}{\int I_1 \nu\, d\nu} \quad (1)$$

where ν_1 and ν_λ are the average wave numbers of $^5D_0 \rightarrow {}^7F_1$ and $^5D_0 \rightarrow {}^7F_\lambda$ transitions, respectively, e is the electronic charge, $\frac{\int I_\lambda \nu\, d\nu}{\int I_1 \nu\, d\nu}$ is the ratio of the integrated intensity of $^5D_0 \rightarrow {}^7F_\lambda$ to the $^5D_0 \rightarrow {}^7F_1$ transition, and $\frac{9n^3}{\eta(\eta^2+2)^2}$ is the Lorentz local field correction and η is the refractive index of the medium. The values of square reduced matrix elements $[\langle\psi J \| U^\lambda \| \psi J'\rangle]^2$ were obtained from the literature.[99,100] The covalence in bonding in the first coordination sphere is directly related to the Ω_2 parameter, and the larger value is an indication of the larger covalent character in the bonding. The higher value of the Ω_2 parameter is also indicative of the higher hypersensitive behavior of the $^5D_0 \rightarrow {}^7F_2$ transition.[101] The Ω_4 parameter provides information regarding the rigidity of the host medium in which Ln(III) ions are located.[102] The $^5D_0 \rightarrow {}^7F_6$ transition is not observed experimentally; thus, the Ω_6 experimental parameter could not be obtained and is neglected in calculations.

The radiative transition probability (A), radiative lifetime τ_{rad}, and emission quantum efficiency Q^{Eu}_{Eu} for the transition of Eu^{3+} in both solution and solid states were calculated using both the Judd–Ofelt theory and experimental results. The radiative transition probability (A) between two manifolds j and j' is given by eq 2

$$A(\psi_j, \psi_{j'}) = \frac{64\pi^4\nu^3}{3h(2j+1)}[\chi D_{ed} + \eta^3 D_{md}] \quad (2)$$

where D_{ed} and D_{md} are the dipole strength of electric and magnetic dipoles, respectively, η is the refractive index, χ is the Lorentz local field correction equaling to $\frac{\eta(\eta^2+2)^2}{9}$, and ν is the average wave number of the transition.

We calculated the radiative transition probability (A) for a transition originating from $^5D_0$ with j equaling to zero to $^7F_\lambda$ with j equaling λ = 0, 1, 2, 3, 4, 5, and 6 from the emission spectra using eq 3

$$A_{0-\lambda} = A_{0-1}\frac{S_{0-\lambda}}{S_{0-1}}\frac{\sigma_\lambda}{\sigma_1} \quad (3)$$

where $S_{0-\lambda}$ and σ_λ are the area under the $0 \rightarrow \lambda$ transition of emission spectra and its energy barycenter, respectively. A_{0-1} is the Einstein coefficient for the $0 \rightarrow 1$ magnetic-dipole transition, and its reported value is 50 s^{-1}.[103] The relationship between lifetime and the transition probabilities (radiative or non-radiative) is given by eq 4

$$A_{tot} = \frac{1}{\tau} = A_{rad} + A_{nrad} \quad (4)$$

where A_{rad} is the summation of all the radiative probabilities for transitions between $^5D_0 \rightarrow {}^7F_\lambda$ with $\lambda = j$ (eq 5)

$$A_{rad} = \sum_{\lambda=j} A_{0-j} \quad (5)$$

The inverse of A_{rad} gives the radiative lifetime τ_{rad} of the $^5D_0$ level and the emission quantum efficiency of the $^5D_0$ level labeled as intrinsic quantum yield Q^{Eu}_{Eu} is given by eq 6

$$Q^{Eu}_{Eu} = \frac{A_{rad}}{A_{rad} + A_{nrad}} \quad (6)$$

The results obtained show that Ω_2 is much higher than Ω_4 in any given solvent, solid state, and thin hybrid films, indicating that the $^5D_0 \rightarrow {}^7F_2$ transition is strongly hypersensitive (Table 7). The ratio of Ω_2:Ω_4 is the lowest for the solid state, indicating that the ligand environment around Eu^{3+} is less polarized in the solid state than in thin hybrid films and solution. This also reflects that the ligand environment around Eu^{3+} is relatively less asymmetric in the solid complex, which agrees with the results obtained from the shape analysis of the crystal structure where the polyhedra around Eu^{3+} ions are less asymmetric. The Ω_4 for the solid Eu^{3+} complex is higher than those in solution and thin films. The higher value could be due to the rigid nature of the solid complex.[102] The relatively smaller value of Ω_4 in the case of solution and hybrid films is indicative of the fact that the lower rank components of the crystal field and dynamic coupling interactions are more

https://doi.org/10.1021/acsomega.0c05976
ACS Omega 2021, 6, 21207–21226

influential than the higher rank components of the crystal field.[76,104]

Experimentally, intensity parameters (Ω_λ) (λ = 2, 4, and 6) of the Eu^{3+} complex are calculated from the Judd−Ofelt theory using the emission spectra and lifetime. Theoretically, the Judd−Ofelt intensity parameters (Ω_λ) are calculated using eqs 7 and 8

$$\Omega_\lambda = (2\lambda + 1) \sum_{t}^{\lambda-1,\lambda+1(\text{odd})} \sum_{p=0}^{t(\text{all})} \frac{|B_{\lambda tp}|^2}{(2t + 1)} \tag{7}$$

where the parameter $B_{\lambda tp}$ is expressed as

$$B_{\lambda tp} = \frac{2}{\Delta E}\langle r^{t+1}\rangle\theta(t, \lambda)\gamma_p^t - \left|\frac{(\lambda + 1)(2\lambda + 3)}{2\lambda + 1}\right|^{1/2} \times \langle r^\lambda\rangle (1 - \sigma_\lambda)\langle f||C^{(\lambda)}||f\rangle \Gamma_p^t\delta_{t,\lambda+1} \tag{8}$$

The theoretical intensity parameters are calculated by adjusting the charge factor (g) and polarizabilities (α) appearing in eqs 9 and 10, respectively, to reproduce the phenomenological (experimental) values for Ω_2 and Ω_4.

$$\gamma_p^t = \left(\frac{4\pi}{2t + 1}\right)^{1/2} e^2 \sum_j \rho_j(2\beta_j)^{t+1}\frac{g_j}{R_j^{t+1}}Y_p^{t*}(\theta_j, \varphi_j) \tag{9}$$

$$\Gamma_p^t = \left(\frac{4\pi}{2t + 1}\right)^{1/2} \sum_j \frac{\alpha_j}{R_j^{t+1}}Y_p^{t*}(\theta_j, \varphi_j) \tag{10}$$

For mononuclear europium complexes, the process of the calculation of theoretical intensity parameters of an optimized structure is a straightforward task and could be obtained by adjusting the charge factor (g) and polarizabilities (α) appearing in eqs 1 and 2, respectively, to reproduce the experimental intensity parameters. However, in the case of complexes containing two or more unique europium centers, the calculation of individual intensity parameters for the unique europium centers by classical procedure produces inconsistent results. The solution to this problem has been presented recently in the form of a theoretical methodology named "overlapped polyhedra method" (OPM).[42] In this method for a di-nuclear molecule, the individual europium coordination polyhedra are overlapped (Figure 14) to reproduce spherical coordinates for all the coordinating atoms with respect to one overlapped europium centers. The charge factor (g) and polarizabilities (α) are then adjusted to reproduce the experimental intensity parameters. Finally, the adjusted charge factor (g) and polarizabilities (α) for individual centers are used to calculate the intensity parameters for the individual centers. The spherical atomic coordinates adjusted charge factor (g) and polarizabilities (α) for the overlapped polyhedra of the crystal structure, Sparkle PM7 and Sparkle RM1, are presented in Tables S9−S11. The calculated intensity parameters, radiative decay probabilities (A_{rad}), non-radiative decay probabilities (A_{nrad}), and intrinsic quantum yields obtained for each polyhedron for the crystal structure, Sparkle PM7 and Sparkle RM1, are presented in Table 8 and

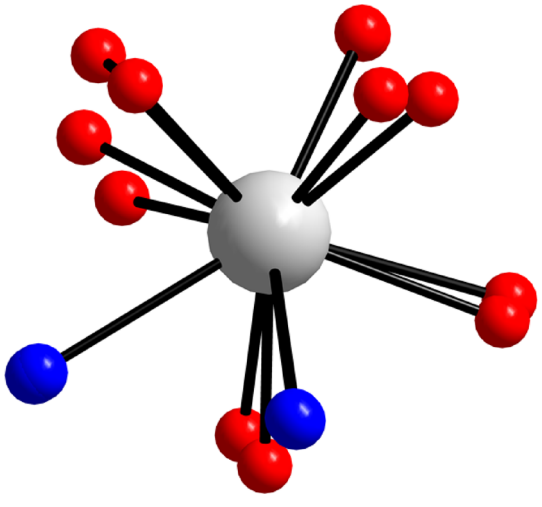

Figure 14. Overlapped polyhedra of the two metal centers.

Table 8. Experimental and Theoretical Intensity Parameters from the OPM, Radiative and Non-radiative Decay Rates (A_{rad} and A_{nrad}), and Intrinsic Quantum Yields

intensity parameters (10^{-20} cm^2)				
			individual adjustment	
	experimental	overlapped method	polyhedron 1	polyhedron 2
Ω_2	20.19	20.19	5.93	6.59
Ω_4	9.98	9.98	4.19	7.72
Ω_6		1.7230	0.9195	0.8270
A_{rad} (S^{-1})	798.67	758.67	242.29	364.84
Q_{Eu}^{Eu} %	56.99	54.14	17.29	26.03

Figures S12 and S13. The intrinsic quantum yields for the individual Eu^{3+} centers of the crystal structure are 17.29% and 26.03%, and their sum is 43.32%. Similarly, the A_{rad} values calculated for the individual Eu^{3+} centers of the crystal structure are 242.29 and 364.84 and their total is 607.13. The total intrinsic quantum yield and A_{rad} are close to the experimental values (Table 7). The agreement between the theoretical and experimental values validates the overlap polyhedra method (OPM) as a reliable tool for the prediction of individual spectroscopic parameters. Similar results where the theoretically calculated values are in agreement with the experimentally obtained data are reported for the dinuclear[42,45] and trinuclear[41] europium complexes. For the optimized (PM7 and RM1) structures, the theoretically calculated total intrinsic quantum yield and A_{rad} are dissimilar to the experimental values, which is due to the different ligand symmetry around the metal ions (Tables S12 and S13). The shapes of the polyhedra around the two Eu^{3+} centers predicted by Sparkle PM7 are similar to those obtained by single-crystal X-ray analysis. However, these are not identical. Sparkle RM1 predicts square antiprismatic geometries around the two Eu^{3+} centers; therefore, the values of the total intrinsic quantum yield and A_{rad} are different from the experimental values.

The radiative branching ratios β_R (ψ_j, ψ_f) could be calculated from the radiative transition probabilities of every transition from the Judd−Ofelt theory using emission spectra and lifetime of the europium complex. The branching ratio of each transition is the ratio of radiative transition probability of that transition to the overall radiative transition probability of the metal ion; in other words, it gives the relative intensity of the transitions and is given as

https://doi.org/10.1021/acsomega.0c05976
ACS Omega 2021, 6, 21207−21226

Table 9. Branching Ratios of the Various Transitions $\beta_{0\text{-}1}$, $\beta_{0\text{-}2}$, and $\beta_{0\text{-}4}$ of $[Eu(fod)_3(\mu\text{-bpp})Eu(fod)_3]$

branching ratio	transitions	acetone	chloroform	dichloromethane	ethanol	solid state	TF10	TF5	RM1	PM7	crystal structure
$\beta_{0\text{-}1}$	$^5D_0 \rightarrow {}^7F_1$	0.086	0.070	0.080	0.092	0.063	0.068	0.071	0.061	0.061	0.061
$\beta_{0\text{-}2}$	$^5D_0 \rightarrow {}^7F_2$	1.096	0.865	0.956	1.082	0.695	0.803	0.793	0.751	0.754	0.751
$\beta_{0\text{-}4}$	$^5D_0 \rightarrow {}^7F_4$	0.044	0.081	0.035	0.045	0.132	0.040	0.046	0.188	0.185	0.188

$$\beta_R(\psi_j, \psi_{j'}) \frac{A(\psi_j, \psi_{j'})}{A_{rad}} \quad (11)$$

The experimentally calculated branching ratios are presented in Table 9. The branching ratio of the transitions follow the order $^5D_0 \rightarrow {}^7F_2 > {}^5D_0 \rightarrow {}^7F_1 > {}^5D_0 \rightarrow {}^7F_4$ in any given solvent as well as in the solid state. The $\beta_{0\text{-}2}$ value of the $^5D_0 \rightarrow {}^7F_2$ transition is the highest in acetone followed by ethanol, dichloromethane, chloroform, PMMA thinfilm@10%(w/w), PMMA thinfilm@5%(w/w), and the solid state. In laser designing, the fluorescence branching ratio is an essential parameter because it characterizes the possibility of attaining a stimulated emission from any specific transition.[105]

3. CONCLUSIONS

In summary, the dinuclear complexes of Sm^{3+} and Eu^{3+} bridged by the bpp ligand were synthesized in good yield. The ^1H NMR and ^1H-^1H COSY techniques were used to assign the proton resonances for the complexes. The shifts induced by paramagnetic centers are dipolar in nature. The photoluminescence of Sm^{3+} and Eu^{3+} complexes was studied in different solvents, the solid state, and polymer-based thin hybrid films. The spectroscopic parameters are calculated both experimentally and theoretically and are found to be in agreement. The overlap polyhedra method (OPM) was used to calculate the individual spectroscopic parameters of two Eu^{3+} sites in the dinuclear $[Eu(fod)_3(\mu\text{-bpp})Eu(fod)_3]$ complex. The Commission Internationale de l'Eclairage (CIE) chromaticity coordinates of the spectra of the complexes in different solvents, solid state, and thin hybrid films show that the Sm^{3+} and Eu^{3+} complexes emit orange and red, respectively. The results of the shape analysis of the coordination polyhedron around the metal ions in the crystal structures of the dinuclear complexes show that the ligand environment symmetries are different around the two centers in a given complex and are distorted dodecahedron and distorted square antiprism. The results of shape analysis using the magnitude of angles method[65] are similar to the results obtained from SHAPE software,[66] indicating that the method is efficacious for shape analysis. The work is in progress and other complexes of the series containing lanthanides are under investigation, and their structures and properties would be reported in future papers.

4. EXPERIMENTAL SECTION AND COMPUTATIONAL METHODS

4.1. Materials. The lanthanide oxides (Ln_2O_3, Ln = La, Sm, Eu and Lu; Sigma-Aldrich 99.9%) were converted into corresponding chlorides $LnCl_3 \cdot nH_2O$ (n = 6−7) by adding an appropriate amount of hydrochloric acid and drying out the product on water bath. 6,6,7,7,8,8,8-Heptafluoro-2,2-dimethyl-3,5-octanedione (Hfod) and 2,3-bis(2-pyridyl)pyrazine (bpp) were also purchased from Sigma-Aldrich. Polymethyl methacrylate (PMMA) with an average molecular weight of 120,000 (Aldrich) was used. AR/spectroscopic grade solvents were used in the study.

4.2. Synthesis. The hydrated $Ln(fod)_3$ chelates (Ln = La, Lu, Sm, and Eu) were synthesized by the literature method.[106,107] The complexes were synthesized by allowing the ethanol solutions of equimolar amounts of chelate and bpp to react (Figure 15). All the complexes were synthesized by a

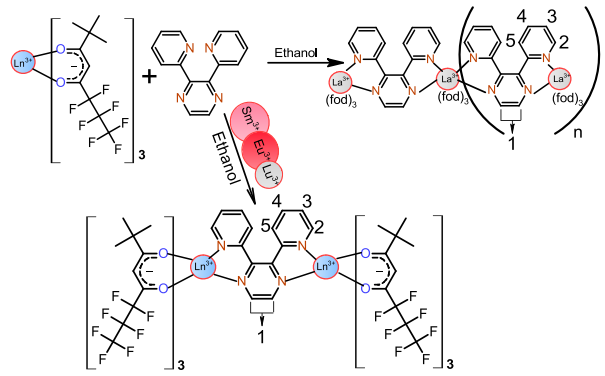

Figure 15. Reaction pathways.

similar method. The synthesis of the Eu^{3+} complex described here is the representative. The reaction of $Eu(fod)_3$ (800 mg; 77.15×10^{-5} moles) and bpp (187.66 mg; 77.15×10^{-5} moles) in equimolar ratio was carried out in 20 mL of ethanol. The reaction mixture was continuously stirred on a magnetic stirrer-cum hot plate at 40 °C for about 8 h. Then, it was left at room temperature for slow evaporation of the solvent. After 3 days, the solid product appeared, which was isolated. The crystals obtained were washed with cold ethanol twice and dried *in vacuo* over P_4O_{10}. The decanted portion of the reaction mixture was also left out at room temperature for complete evaporation of the solvent. Upon complete evaporation of the poured-out liquid, the solid obtained was found to be unreacted bpp since it melts between 168 and 170 °C (the melting point of bpp is in the range of 168−170 °C). The amount left was around 50% of the initial amount used. It suggests that only one mole of bpp reacts with two moles of $[Eu(fod)_3]$ and the reaction takes place in a 1:2 molar ratio (bpp:$Eu(fod)_3$), resulting in the formation of dinuclear complexes. However, in the case of the lanthanum complex, no unreacted bpp was recovered, suggesting a 1:1 reaction between $[La(fod)_3]$ and bpp.

4.3. Characterization. Elemental analysis of the complexes was carried out on an Elementar modern elemental analyzer type vario EL cube. Melting points were obtained by a conventional capillary method and DSC of the samples (DSC 6220 SIINT, Japan). The TGA/DTA results of the complexes were obtained in an inert atmosphere under nitrogen gas (N_2) with a heating rate of 10 °C per minute on an Exstar 6000 TGA/DTA from SIINT, Japan. The infrared spectra were recorded on a BRUKER FT-IR spectrophotometer in the range of 600−4000 cm^{-1}. The mass spectra of the complexes in positive ion reflector mode were recorded on a Bruker

https://doi.org/10.1021/acsomega.0c05976
ACS Omega 2021, 6, 21207−21226

autoflex TOF/TOF FLEX-PC mass spectrometer. Powder X-ray diffraction (XRD) pattern of the complexes were elucidated on Phillips Analytica PW 1830 instrument (Philips, Netherlands) with monochromatic Cu Kα1 radiation. The ^{1}H NMR and ^{1}H-^{1}H COSY spectra of the diamagnetic and paramagnetic complexes were recorded at 298 K on the BRUKER Avance II 500 MHz NMR spectrometer in $CDCl_3$. The Horiba Jobin Yvon Fluorolog 3-22 spectrofluorometer equipped with a 450 W xenon lamp as the excitation source and a R928P Hamamatsu photomultiplier tube as the detector were used to obtain the steady-state luminescence and excitation spectra. The lifetime of the excited states of the complexes was measured on an Edinburgh FLS920 spectrophotometer. The absorption spectra were obtained on a Perkin-Elmer Lambda-40 spectrophotometer in a 1 cm^3 stoppered quartz cell.

[La(fod)$_3$(bpp)] Color: white; melting point: 120 °C; yield: 95%; elemental analysis: calculated (found): carbon 41.99(41.43), hydrogen 3.20(3.18), and nitrogen 4.45(4.33). IR (KBr; cm^{-1}): 3100−2850 cm^{-1}, aromatic ν_{as}(C−H) and ν_s(C−H); 1613 cm^{-1}, ν_s(C═O); 1505 cm^{-1}, ν_s(C═C); 1150−1250 cm^{-1}, ν_s(C−F). ^{1}H NMR (500 MHz, $CDCl_3$); δ 8.99 ppm (2H, s), 8.86 (2H, s), 7.04 (2H, m), 7.70 (2H, t), 7.39 (2H, m), 5.88 (3H, s), 1.05 (27H, s).

[Sm(fod)$_3$(μ-bpp)Sm(fod)$_3$] Color: white; melting point: 137 °C; yield: 95%; elemental analysis: calculated (found): carbon 38.55(38.36), hydrogen 3.06(3.05), and nitrogen 2.43(2.41). IR (KBr; cm^{-1}): 3100−2850 cm^{-1}, aromatic ν_{as}(C−H) and ν_s(C−H); 1614 cm^{-1}, ν_s(C═O); 1505 cm^{-1}, ν_s(C═C); 1150−1250 cm^{-1}, ν_s(C−F). ^{1}H NMR (500 MHz, $CDCl_3$); δ 7.16 ppm (2H, s), 6.23 (2H, d), 7.21 (2H, t), 7.04 (8H, s), 8.11 (2H, s), 1.01 (54H, s).

[Eu(fod)$_3$(μ-bpp)Eu(fod)$_3$] Color: white; melting point: 140 °C; yield: 95%; elemental analysis: calculated (found): carbon 38.50(38.24), hydrogen 3.05(3.05), and nitrogen 2.43(2.44). IR (KBr; cm^{-1}): 3100−2850 cm^{-1}, aromatic ν_{as}(C−H) and ν_s(C−H); 1614 cm^{-1}, ν_s(C═O); 1506 cm^{-1}, ν_s(C═C); 1150−1250 cm^{-1}, ν_s(C−F). ^{1}H NMR (500 MHz, $CDCl_3$); δ 16.98 ppm (2H, s), 17.72 (2H, s), 15.14 (2H, s), 11.78 (2H, s), 10.23 (2H, s), 2.59 (6H, s), 1.41 (54H, s).

[Lu(fod)$_3$(μ-bpp)Lu(fod)$_3$] Color: white; melting point: 144 °C; yield: 95%; elemental analysis: calculated (found): carbon 37.75(37.41), hydrogen 2.98(2.97), and nitrogen 2.38(2.38). IR (KBr; cm^{-1}): 3100−2850 cm^{-1}, aromatic ν_{as}(C−H) and ν_s(C−H); 1615 cm^{-1}, ν_s(C═O); 1506 cm^{-1}, ν_s(C═C); 1150−1250 cm^{-1}, ν_s(C−F). ^{1}H NMR (500 MHz, $CDCl_3$); δ 9.32 ppm (2H, s), 9.25 (2H, s), 7.67 (2H, s), 7.47 (4H, t), 5.87 (6H, s), 1.06 (54H, s).

The strong O−H stretching vibrations appearing in the range of 3500−3700 cm^{-1} in the IR spectra of the chelates have disappeared from the spectra of the complexes, suggesting that the water molecules present in the chelates are replaced by the ancillary ligand upon coordination (Figures S38−S41). It is strong evidence that the bpp ligand has coordinated to the chelate. The strong bands appearing in the complexes at 1515 ± 5 cm^{-1} and 1620 ± 5 cm^{-1} are assigned to C═O and C═C stretching vibrations and are characteristics of lanthanide β-diketonate complexes.[108,109] These bands are shifted toward the lower energy side as compared to their position in the chelates. Similarly, the bands appearing around 1550, 1405, 1062, 870, and 787 cm^{-1} in the chelates have also been shifted in the complexes. Most of the characteristic IR bands of the bpp could not be observed since these are obscured by the strong chelate absorptions. The characteristic C═N and C═C ring stretching vibrations of free bpp appearing at 1583 cm^{-1}[110] has been reported to shift to a higher wave number when bpp acts as the bridging ligand by exploiting the two NN chelating sites.[54] We could not observe this stretching vibration, perhaps it has merged with the strong band appearing at 1620 cm^{-1}. This is consistent with the binding of the bpp to two metal centers through its two NN chelating sites.[55,111] The strong bands[112,113] appearing in the region of 1108−1278 cm^{-1} are assigned to the C−F stretching vibrations of the β-diketone. These C−F bands show a smaller shift from their positions in the chelates on complex formation, which could be due to the non-proximity to the metal.

The powder XRD spectra of the complexes reveal that the samarium and europium complexes are crystalline in nature, while the lanthanum complex is semicrystalline (Figure S42). The ESI$^+$-MS spectra of the complexes were obtained in chloroform solution (Figures S43−S46). The molecular ion peak for the complexes could not be observed. However, the peaks corresponding to the molecular fragments Ln(fod)$_2$bpp and Ln(fod)$_2$(bpp)$_2$ are apparent in the spectra. The easy splitting of CF_3 fragments and the possible migration of fluorine atoms[114,115] results in various types of molecular fragments.

The thermograms (TGA and DTA) of the complexes are recorded in the temperature range of 40−500 °C and are shown in Figures S47 and S48. The lanthanide complexes with fluorinated β-diketone like Hfod and hexafluoroacetylacetone (Hhfac) are found to be thermally stable and evaporate without decomposition.[21−26,106] The complexes under study do not show any thermal degradation and evaporate in the temperature range of 300−340 °C. The single-step volatilization reveals that the complexes do not dissociate, and the ancillary ligand and β-diketone moieties remain coordinated in the vapor. The DTA curves of the complexes show two endothermic peaks: one at the lower temperature represents melting of the complexes (phase transformation) and the other between 321 °C and 324 °C represent the volatilization. The melting points noted from the DTA and DSC (Figure S49) curves are well in line with those obtained from the conventional capillary method.

4.4. Single-Crystal Structure Analysis. Single-crystal X-ray data collection was performed on a Bruker SMART APEX CCD diffractometer equipped with a fine focus 1.75 kW sealed-tube Mo Kα X-ray source (λ = 0.71073 Å) with increasing ω (width of 0.3° per frame) at a scan speed of 5 s frame^{-1}. All measurements were performed at liquid nitrogen temperature, 100 K. Intensity data were collected using the ω-2θ scan mode and corrected for Lorentz-polarization and absorption effects.[116] The structures were solved with the ShelXT (Sheldrick, 2015),[117] using olex2 software.[118] The structure solution using a direct method were obtained with SHELXL-2018/3.[119] The non-hydrogen atoms were refined with anisotropic displacement coefficients, and their coordinates were permitted to ride on their respective carbon atoms. For all the atoms, the atomic positions, for all the non-hydrogen atoms, the anisotropic thermal parameters, and for all the hydrogen atoms, the isotropic thermal parameters, were included in the final refinement. The perspective views were obtained using ORTEP.[120] The crystal code provided by CCDC are 1956378 for [Sm(fod)$_3$(μ-bpp)Sm(fod)$_3$] and 1956379 for [Eu(fod)$_3$(μ-bpp)Eu(fod)$_3$]. The crystal model showed signs of disorder, and some alternative positions were

https://doi.org/10.1021/acsomega.0c05976
ACS Omega 2021, 6, 21207−21226

found for terminal groups. The higher $R1$ and w$R2$ values for the complexes are mostly due to the disorder in the tertiary butyl and perfluoryl groups of the fod moiety. These observations are similar to those reported for the crystal structures of the complexes containing fod, [Eu(fod)$_3$(phen)],[88] [Dy(fod)$_3$(phen)],[20] and other similar complexes.[112,121]

4.5. Computational Details. The ground state geometry of samarium and europium complexes were elucidated using Sparkle/PM7[36] and RM1[37] implemented in the MOPAC2016 software package.[122] The input structures were drawn and were pre-optimized by the molecular mechanics (AMBER model) implemented in Gabedit software.[123] The vibrational frequencies of all the optimized structures were calculated to check that the optimized structures are at the local minimum. The keywords used were GNORM = 0.25; PRECISE; GEO-OK; XYZ (for Cartesian coordinates); T = 10D; ALLVEC; SPARKLE BFGS; and 1SCF for MOPAC2016 to not change or attempt to optimize the starting crystallography geometry. Of the various Sparkle models implemented in the MOPAC2016, the Sparkle RM1 and PM7 provided the comprehensive structure of the complexes. The reason for the selection of a particular Sparkle model depends upon the impact of that model on the quantum chemical modeling of the organic ligand(s) (β-diketone and ancillary ligand) present in the complex.[38]

4.6. Thin Film Formation. Thin hybrid films of the complexes were obtained by the drop casting technique on the glass slides.[97] The quartz glass slides were first washed with a solution of NH_3 and H_2O_2 (50%: 50%) and then were dipped into concentrated HCl for 10 min, and finally, these were washed thoroughly with double distilled water. The 5% and/or 10% (w/w) solution of the complex and PMMA was prepared in chloroform.

■ ASSOCIATED CONTENT

Supporting Information

The Supporting Information is available free of charge at https://pubs.acs.org/doi/10.1021/acsomega.0c05976.

Single-crystal X-ray details for the Sm^{3+} complex (CIF)
Single-crystal X-ray details for the Eu^{3+} complex (CIF)
The characterization spectra and data tables, Sparkle RM1 and PM7 optimized structures, photophysical spectra and data tables, lifetime spectra, and CIE color coordinate diagrams (PDF)

■ AUTHOR INFORMATION

Corresponding Author

Khalid Iftikhar − *Lanthanide Research Laboratory, Department of Chemistry, Jamia Millia Islamia, New Delhi 110025, India;* orcid.org/0000-0002-5987-3901; Email: kiftikhar@jmi.ac.in

Author

Aabid Bashir Ganaie − *Lanthanide Research Laboratory, Department of Chemistry, Jamia Millia Islamia, New Delhi 110025, India*

Complete contact information is available at: https://pubs.acs.org/10.1021/acsomega.0c05976

Notes

The authors declare no competing financial interest.

■ ACKNOWLEDGMENTS

A.B.G. thanks CSIR (Govt. of India) for a Senior Research Fellowship. The authors are thankful to Dr. M. Kausar Raza of Indian Institute of Science (IISC), Bangalore, for providing the single-crystal X-ray structures of the complexes, and we are also grateful to Dr. Neetu Singh of Advance Instrumentation Research Facility (AIRF), JNU, New Delhi, for time-resolved fluorescence. The Central Instrumentation Facility (CIF) of Jamia Millia Islamia is also gratefully acknowledged for extending FT-IR and steady-state luminescence facility. This work was not funded by any agency.

■ REFERENCES

(1) Bradley, J. D. B.; Pollnau, M. Erbium-Doped Integrated Waveguide Amplifiers and Lasers. *Laser Photon. Rev.* **2011**, *5*, 368−403.
(2) Sage, I.; Bourhill, G. Triboluminescent Materials for Structural Damage Monitoring. *J. Mater. Chem.* **2001**, *11*, 231−245.
(3) Fueyo-González, F.; Garcia-Fernandez, E.; Martínez, D.; Infantes, L.; Orte, A.; González-Vera, J. A.; Herranz, R. Smart Lanthanide Antennas for Sensing Water. *Chem. Commun.* **2020**, *56*, 5484−5487.
(4) Parker, D.; Williams, J. A. G. Getting Excited About Lanthanide Complexation Chemistry. *J. Chem. Soc., Dalton Trans.* **1996**, *18*, 3613−3628.
(5) Amoroso, A. J.; Pope, S. J. A. Using Lanthanide Ions in Molecular Bioimaging. *Chem. Soc. Rev.* **2015**, *44*, 4723−4742.
(6) Chen, J.; Xie, Z.; Meng, L.; Hu, Z.; Kuang, X.; Xie, Y.; Lu, C. Z. Luminescence Tunable Europium and Samarium Complexes: Reversible On/Off Switching and White-Light Emission. *Inorg. Chem.* **2020**, *59*, 6963−6977.
(7) Yang, Y.; Chen, L.; Jiang, F.; Yu, M.; Wan, X.; Zhang, B.; Hong, M. A Family of Doped Lanthanide Metal-Organic Frameworks for Wide-Range Temperature Sensing and Tunable White Light Emission. *J. Mater. Chem. C* **2017**, *5*, 1981−1989.
(8) Lapaev, D. V.; Nikiforov, V. G.; Lobkov, V. S.; Knyazev, A. A.; Galyametdinov, Y. G. A Photostable Vitrified Film Based on a Terbium(iii) β-Diketonate Complex as a Sensing Element for Reusable Luminescent Thermometers. *J. Mater. Chem. C* **2018**, *6*, 9475−9481.
(9) Mathieu, E.; Sipos, A.; Demeyere, E.; Phipps, D.; Sakaveli, D.; Borbas, K. E. Lanthanide-Based Tools for the Investigation of Cellular Environments. *Chem. Commun.* **2018**, *54*, 10021−10035.
(10) Bünzli, J.-C. G.; Piguet, C. Taking Advantage of Luminescent Lanthanide Ions. *Chem. Soc. Rev.* **2005**, *34*, 1048.
(11) Bünzli, J.-C. G. Benefiting From The Unique Properties of Lanthanide Ions. *Acc. Chem. Res.* **2006**, *39*, 53−61.
(12) Bünzli, J. C. G. Lanthanide Photonics: Shaping the Nanoworld. *Trends Chem.* **2019**, *1*, 751−762.
(13) Weissman, S. I. Intramolecular Energy Transfer the Fluorescence of Complexes of Europium. *J. Chem. Phys.* **1942**, *10*, 214−217.
(14) Kalyakina, A. S.; Utochnikova, V. V.; Zimmer, M.; Dietrich, F.; Kaczmarek, A. M.; Van Deun, R.; Vashchenko, A. A.; Goloveshkin, A. S.; Nieger, M.; Gerhards, M.; et al. Remarkable High Efficiency of Red Emitters Using Eu(iii) Ternary Complexes. *Chem. Commun.* **2018**, *54*, 5221−5224.
(15) Manzur, J.; Poblete, C.; Morales, J.; De Santana, R. C.; Queiroz Maia, L. J.; Vega, A.; Fuentealba, P.; Spodine, E. Enhancement of Terbium(III)-Centered Luminescence by Tuning the Triplet Energy Level of Substituted Pyridylamino-4-R-Phenoxo Tripodal Ligands. *Inorg. Chem.* **2020**, *59*, 5447−5455.
(16) Binnemans, K. Rare-Earth Beta-Diketonates. In *Handbook on the physics and chemistry of rare earths*; 2005; Vol. 35, pp. 107−272.
(17) Malta, O. L.; Brito, H. F.; Menezes, J. F. S.; Gonçalves e Silva, F. R.; De Mello Donegá, C.; Alves, S., Jr. Experimental and Theoretical Emission Quantum Yield in the Compound Eu-

(thenoyltrifluoroacetonate)$_3$.2(dibenzyl sulfoxide). *Chem. Phys. Lett.* **1998**, *282*, 233−238.
(18) Moudam, O.; Rowan, B. C.; Alamiry, M.; Richardson, P.; Richards, B. S.; Jones, A. C.; Robertson, N. Europium Complexes With High Total Photoluminescence Quantum Yields in Solution and in PMMA. *Chem. Commun.* **2009**, *43*, 6649−6651.
(19) HemmilÄ, I.; Mukkala, V.-M.; Takalo, H. Effect of C-H bonds on the Quenching of Luminescent Lanthanide Chelates. *J. Fluoresc.* **1995**, *5*, 159−163.
(20) Gao, C.; Yang, Q.; Wang, B. W.; Wang, Z. M.; Gao, S. Evaporable Lanthanide Single-Ion Magnet. *CrystEngComm* **2016**, *18*, 4165−4171.
(21) Ahmed, Z.; Iftikhar, K. Red, Orange-Red and near-Infrared Light Emitting Ternary Lanthanide Tris β-Diketonate Complexes with Distorted C_{4v} Geometrical Structures. *J. Chem. Soc., Dalton Trans.* **2019**, *48*, 4973−4986.
(22) Ahmed, Z.; Iftikhar, K. Efficient Layers of Emitting Ternary Lanthanide Complexes for Fabricating Red, Green, and Yellow OLEDs. *Inorg. Chem.* **2015**, *54*, 11209−11225.
(23) Ahmed, Z.; Iftikhar, K. Sensitization of Visible and NIR Emitting Lanthanide(III) Ions in Noncentrosymmetric Complexes of Hexafluoroacetylacetone and Unsubstituted Monodentate Pyrazole. *J. Phys. Chem. A* **2013**, *117*, 11183−11201.
(24) Bhat, S. A.; Iftikhar, K. Synthesis, Characterization, Photoluminescence and Intensity Parameters of High Quantum Efficiency Pure-Red Emitting Eu(III) Fluorinated β-Diketone Complexes. *New J. Chem.* **2019**, *43*, 13162−13172.
(25) Irfanullah, M.; Iftikhar, K. Photoluminescence, Optical Absorption and Hypersensitivity in Mono- and Dinuclear Lanthanide (TbIII and HoIII) β-Diketonate Complexes with Diimines and Bis-Diimine Bridging Ligand. *J. Lumin.* **2010**, *130*, 1983−1993.
(26) Irfanullah, M.; Iftikhar, K. Synthesis and Spectroscopic Analysis of an Extended Series of Hetero Dinuclear Complexes Containing Two Different Lanthanides in 1:1 Stoichiometry. *Inorg. Chim. Acta* **2013**, *394*, 373−384.
(27) Ayscue, R. L., III; Verwiel, C. P.; Bertke, J. A.; Knope, K. E. Excitation-Dependent Photoluminescence Color Tuning in Lanthanide-Organic Hybrid Materials. *Inorg. Chem.* **2020**, *59*, 7539−7552.
(28) Wei, C.; Sun, B.; Zhao, Z.; Cai, Z.; Liu, J.; Tan, Y.; Wei, H.; Liu, Z.; Bian, Z.; Huang, C. A Family of Highly Emissive Lanthanide Complexes Constructed with 6-(Diphenylphosphoryl)Picolinate. *Inorg. Chem.* **2020**, *59*, 8800−8808.
(29) Ullmann, S.; Hahn, P.; Blömer, L.; Mehnert, A.; Laube, C.; Abel, B.; Kersting, B. Dinuclear Lanthanide Complexes Supported by a Hybrid Salicylaldiminato/Calix[4]Arene-Ligand: Synthesis, Structure, and Magnetic and Luminescence Properties of $(HNEt_3)$-$[Ln_2(HL)(L)]$ (Ln = SmIII, EuIII, GdIII, TbIII). *Dalton Trans.* **2019**, *48*, 3893−3905.
(30) Ullmann, S.; Hahn, P.; Mini, P.; Tuck, K. L.; Kahnt, A.; Abel, B.; Gutierrez Suburu, M. E.; Strassert, C. A.; Kersting, B. Mixed-Ligand Lanthanide Complexes Supported by Ditopic Bis(Imino-Methyl)-Phenol/Calix[4]Arene Macrocycles: Synthesis, Structures, and Luminescence Properties of $[Ln_2(L_2)(MeOH)_2]$ (Ln = La, Eu, Tb, Yb). *Dalton Trans.* **2020**, *49*, 11179−11191.
(31) Shavaleev, N. M.; Eliseeva, S. V.; Scopelliti, R.; Bünzli, J.-C. G. Designing Simple Tridentate Ligands for Highly Luminescent Europium Complexes. *Chem. - Eur. J.* **2009**, *15*, 10790−10802.
(32) Lo, W.-S.; Zhang, J.; Wong, W.-T.; Law, G.-L. Highly Luminescent Sm III Complexes with Intraligand Charge-Transfer Sensitization and the Effect of Solvent Polarity on Their Luminescent Properties. *Inorg. Chem.* **2015**, *54*, 3725−3727.
(33) Melo, L. L. L. S.; Castro, G. P., Jr.; Gonçalves, S. M. C. Substantial Intensification of the Quantum Yield of Samarium(III) Complexes by Mixing Ligands: Microwave-Assisted Synthesis and Luminescence Properties. *Inorg. Chem.* **2019**, *58*, 3265−3270.
(34) Cuan, J.; Yan, B. Luminescent Lanthanide-Polyoxometalates Assembling Zirconia-Alumina-Titania Hybrid Xerogels through Task-Specified Ionic Liquid Linkage. *RSC Adv.* **2014**, *4*, 1735−1743.
(35) Rodrigues, D. A.; da Costa, N. B., Jr.; Freire, R. O. Would The Pseudocoordination Centre Method be Appropriate to Describe the Geometries of Lanthanide Complexes. *J. Chem. Inf. Model.* **2011**, *51*, 45−51.
(36) Filho, M. A. M.; Dutra, J. D. L.; Rocha, G. B.; Freire, R. O.; Simas, A. M. Sparkle/RM1 Parameters for the Semiempirical Quantum Chemical Calculation of Lanthanide Complexes. *RSC Adv.* **2013**, *3*, 16747.
(37) Dutra, J. D. L.; Filho, M. A. M.; Rocha, G. B.; Freire, R. O.; Simas, A. M.; Stewart, J. J. P. Sparkle/PM7 Lanthanide Parameters for the Modeling of Complexes and Materials. *J. Chem. Theory Comput.* **2013**, *9*, 3333−3341.
(38) Dutra, J. D. L.; Freire, R. O. Theoretical Tools for the Calculation of the Photoluminescent Properties of Europium Systems − A case study. *J. Photochem. Photobiol., A* **2013**, *256*, 29−35.
(39) Marques, L. F.; Santos, H. P.; D'Oliveira, K. A.; Botezine, N. P.; Freitas, M. C. R.; Freire, R. O.; Dutra, J. D. L.; Martins, J. S.; Legnani, C.; Quirino, W. G.; et al. New Photo/electroluminescent Europium-(III) β-Diketonate Complex Containing a *p,p′*-Disubstituted Bipyridine Ligand: Synthesis, Solid State Characterization, Theoretical and Experimental Spectroscopic Studies. *Inorg. Chim. Acta* **2017**, *458*, 28−38.
(40) Marques, L. F.; Correa, C. C.; Garcia, H. C.; Martins Francisco, T.; Ribeiro, S. J. L.; Dutra, J. D. L.; Freire, R. O.; Machado, F. C. Theoretical and Experimental Spectroscopic Studies of the First Highly Luminescent Binuclear Hydrocinnamate of Eu(III), Tb(III) and Gd(III) with bidentate 2,2′-bipyridine Ligand. *J. Lumin.* **2014**, *148*, 307−316.
(41) Monteiro, J. H. S. K.; Dutra, J. D. L.; Freire, R. O.; Formiga, A. L. B.; Mazali, I. O.; de Bettencourt-Dias, A.; Sigoli, F. A. Estimating the Individual Spectroscopic Properties of Three Unique Eu^{III} Sites in a Coordination polymer. *Inorg. Chem.* **2018**, *57*, 15421−15429.
(42) Dutra, J. D. L.; Ferreira, J. W.; Rodrigues, M. O.; Freire, R. O. Theoretical Methodologies for Calculation of Judd−Ofelt Intensity Parameters of Polyeuropium Systems. *J. Phys. Chem. A* **2013**, *117*, 14095−14099.
(43) Rodrigues, M. O.; da Costa Júnior, N. B.; de Simone, C. A.; Araújo, A. A. S.; Brito-Silva, A. M.; Paz, F. A. A.; de Mesquita, M. E.; Júnior, S. A.; Freire, R. O. Theoretical and Experimental Studies of the Photoluminescent Properties of the Coordination Polymer $[Eu(DPA)(HDPA)(H_2O)_2]\cdot 4H_2O$. *J. Phys. Chem. B* **2008**, *112*, 4204−4212.
(44) Rodrigues, M. O.; Paz, F. A. A.; Freire, R. O.; de Sá, G. F.; Galembeck, A.; Montenegro, M. C. B. S. M.; Araújo, A. N.; Alves, S., Jr. Modeling, Structural, and Spectroscopic Studies of Lanthanide-Organic Frameworks. *J. Phys. Chem. B* **2009**, *113*, 12181−12188.
(45) Rodrigues, C. V.; Luz, L. L.; Dutra, J. D. L.; Junior, S. A.; Malta, O. L.; Gatto, C. C.; Streit, H. C.; Freire, R. O.; Wickleder, C.; Rodrigues, M. O. Unusual Photoluminescence Properties of the 3D Mixed-Lanthanide-Organic Frameworks Induced by Dimeric Structures: A Theoretical and Experimental Approach. *Phys. Chem. Chem. Phys.* **2014**, *16*, 14858−14866.
(46) Alexandropoulos, D. I.; Schulte, K. A.; Vignesh, K. R.; Dunbar, K. R. Slow Magnetic Dynamics in a Family of Mononuclear Lanthanide Complexes Exhibiting the Rare Cubic Coordination Geometry. *Chem. Commun.* **2018**, *54*, 10136−10139.
(47) Vicentini, G.; Zinner, L. B.; Zukerman-Schpector, J.; Zinner, K. Luminescence and Structure of Europium Compounds. *Coord. Chem. Rev.* **2000**, *196*, 353−382.
(48) Monteiro, J. H. S. K.; de Bettencourt-Dias, A.; Sigoli, F. A. Estimating the Donor-Acceptor Distance to Tune the Emission Efficiency of Luminescent Lanthanide Compounds. *Inorg. Chem.* **2017**, *56*, 709−712.
(49) Judd, B. R. Optical Absorption Intensities of Rare-Earth Ions. *Phys. Rev.* **1962**, *127*, 750−761.
(50) Ofelt, G. S. Intensities of Crystal Spectra of Rare-Earth Ions. *J. Chem. Phys.* **1962**, *37*, 511−520.

https://doi.org/10.1021/acsomega.0c05976
ACS Omega 2021, 6, 21207−21226

(51) Balzani, V.; Juris, A.; Venturi, M.; Campagna, S.; Serroni, S. Luminescent and Redox-Active Polynuclear Transition Metal Complexes. *Chem. Rev.* **1996**, *96*, 759−834.
(52) Campagna, S.; Denti, G.; De Rosa, G.; Sabatino, L.; Ciano, M.; Balzani, V. Syntheses, Absorption Spectra, Luminescence Properties, and Electrochemical Behavior of Mono- and Binuclear Ruthenium(II) Complexes of Isomeric Bis(2-Pyridyl)Pyrazines. *Inorg. Chem.* **1989**, *28*, 2565−2570.
(53) Ruminski, R. R.; Wallace, I. Synthesis and Characterization of Chromium and Tungsten Tetracarbonyl Bound to the Bridging Ligand 2,3-Bis(2-Pyridyl)Pyrazine (Dpp). *Polyhedron* **1987**, *6*, 1673−1676.
(54) Thomas, N. C.; Cox, J. Synthesis of Monometallic and Bimetallic 2,2′-Bipyrimidine and 2,3-Bis(2-Pyridyl)Pyrazine Complexes of Ruthenium, Platinum and Palladium. *Polyhedron* **1988**, *7*, 731−735.
(55) Grove, H.; Sletten, J.; Julve, M.; Lloret, F.; Lezama, L. Chains and Channels in Polynuclear Copper(II) Complexes with 2,3-Bis(2-Pyridyl)Pyrazine (Dpp) as Bridging Ligand; Syntheses, Crystal Structures and Magnetic Properties. *Inorg. Chim. Acta* **2000**, *310*, 217−226.
(56) Grove, H.; Julve, M.; Lloret, F.; Kruger, P. E.; Törnroos, K. W.; Sletten, J. Syntheses, Crystal Structures and Magnetic Properties of Copper(II) Polynuclear and Dinuclear Compounds with 2,3-Bis(2-Pyridyl)Pyrazine (Dpp) and Pseudohalide as Ligands. *Inorg. Chim. Acta* **2001**, *325*, 115−124.
(57) Shoup, M.; Hall, B.; Ruminski, R. R. Synthesis, Characterization, and Solvatochromic Studies of Group 6 Metal Carbonyls Bound to the Bridging Ligand 2,3-Bis(2-Pyridyl)Pyrazine (Dpp). *Inorg. Chem.* **1988**, *27*, 200−203.
(58) Ruminski, R.; Cambron, R. T. Synthesis and characterization of rhenium(I) complexes bound to the bridging ligand 2,3-bis(2-pyridyl)pyrazine. *Inorg. Chem.* **1990**, *29*, 1575−1578.
(59) Shavaleev, N. M.; Moorcraft, L. P.; Pope, S. J. A.; Bell, Z. R.; Faulkner, S.; Ward, M. D. Sensitized Near-Infrared Emission from Complexes of Yb^{III}, Nd^{III} and Er^{III} by Energy-Transfer from Covalently Attached PtII-Based Antenna Units. *Chem. - Eur. J.* **2003**, *9*, 5283−5291.
(60) Kennedy, F.; Shavaleev, N. M.; Koullourou, T.; Bell, Z. R.; Jeffery, J. C.; Faulkner, S.; Ward, M. D. Sensitised Near-Infrared Luminescence from Lanthanide(Iii) Centres Using Re(i) and Pt(Ii) Diimine Complexes as Energy Donors in d−f Dinuclear Complexes Based on 2,3-Bis(2-Pyridyl)Pyrazine. *Dalton Trans.* **2007**, 1492−1499.
(61) Sultan, R.; Gadamsetti, K.; Swavey, S. Synthesis, Electrochemistry and Spectroscopy of Lanthanide(III) Homodinuclear Complexes Bridged by Polyazine Ligands. *Inorg. Chim. Acta* **2006**, *359*, 1233−1238.
(62) Viviani, S.; Fratini, A.; Swavey, S. The Effect of the Lanthanide Contraction on Coordination with the Polyazine Bridging Ligand 2,3-Bis(2-Pyridyl)Pyrazine (Dpp). *Inorg. Chem. Commun.* **2012**, *24*, 29−31.
(63) Swavey, S.; Fratini, A.; Grewal, J.; Hutchinson, A. Monometallic Europium, Terbium, and Neodymium Complexes Formed from the Bridging Ligand 2,3-Bis(2-Pyridyl)Pyrazine: Crystal Structure and Temperature Dependent Luminescent Properties. *Inorg. Chim. Acta* **2015**, *428*, 27−31.
(64) Huang, N. T.; Pennington, W. T.; Petersen, J. D. Structure of 2,3-Bis(2-Pyridyl)Pyrazine. *Acta Crystallogr., Sect. C: Cryst. Struct. Commun.* **1991**, *47*, 2011−2012.
(65) Haigh, C. W. A New Simple Criterion for Distinguishing the Types of Structures in Eight-Coordinate Complexes: The Pattern of Bond Angles. *Polyhedron* **1995**, *14*, 2871−2878.
(66) Llunell, M.; Casanova, D.; Cirera, J.; Bofill, P. A. *SHAPE (version 2.1)*; Barcelona, 2013.
(67) Iftikhar, K. Mixed-Ligand Lanthanide Complexes-IX NMR Spectral Study of the Adducts of $Ln(fod)_3$ with 2,2′-Bipyridyl and 1,10-Phenanthroline. *Polyhedron* **1996**, *15*, 1113−1120.
(68) Bleaney, B. Nuclear Magnetic Resonance Shifts in Solution Due to Lanthanide Ions. *J. Magn. Reson.* **1972**, *8*, 91−100.
(69) Eaton, D. R. The Nuclear Magnetic Resonance of Some Paramagnetic Transition Metal Acetylacetonates. *J. Am. Chem. Soc.* **1965**, *87*, 3097−3102.
(70) Horinouchi, S.; Wada, M.; Ishihara, K.; Eguchi, M.; Zhang, G.; Ishikawa, T.; Watanabe, A.; Wang, L.; Ogata, N. Fabrication and Characterization of Rare-Earth Metal-Chelate-Doped Plastic Film and Fiber Materials: Eu(3+)-Chelate-Doped PMMA. *Mater. Devices Opt. Wireless Commun.* **2002**, *4905*, 126.
(71) Karabulut, Y.; Ayvacıklı, M.; Canimoglu, A.; Guinea, J. G.; Kotan, Z.; Ekdal, E.; Akyuz, O.; Can, N. Synthesis and Luminescence Properties of Trivalent Rare-Earth Element-Doped Calcium Stannate Phosphors. *Spectrosc. Lett.* **2014**, *47*, 630−641.
(72) Zucchi, G.; Le Goff, X. F. Magneto-Structural and Photophysical Investigations on a Dinuclear Sm(III) Complex Featuring 2,2′-Bipyrimidine. *Inorg. Chim. Acta* **2012**, *380*, 354−357.
(73) Monteiro, J. H. S. K.; Mazali, I. O.; Sigoli, F. A. Determination of Judd-Ofelt Intensity Parameters of Pure Samarium(III) Complexes. *J. Fluoresc.* **2011**, *21*, 2237−2243.
(74) Horrocks, W. D.; Albin, M. *Progress in Inorganic Chemistry*; Lippard, S. J. Ed.; Progress in Inorganic Chemistry; John Wiley & Sons, Inc.: Hoboken, NJ, USA, 1984.
(75) Kirby, A. F.; Richardson, F. S. Detailed Analysis of the Optical Absorption and Emission Spectra of Europium(3+) in the Trigonal (C_3) $Eu(dbm)_3.H_2O$ System. *J. Phys. Chem.* **1983**, *87*, 2544−2556.
(76) Görller-Walrand, C.; Binnemans, K. Chapter 167 *Spectral Intensities of f-f Transitions*; 1998; Vol. *25*, pp. 101−264.
(77) dos Santos, E. R.; dos Santos, M. A. C.; Freire, R. O.; Júnior, S. A.; Barreto, L. S.; de Mesquita, M. E. On the Use of Theoretical Tools in the Study of Photophysical Properties of the New $Eu(fod)_3$ Complex with Diphenbipy. *Chem. Phys. Lett.* **2006**, *418*, 337−341.
(78) Irfanullah, M.; Iftikhar, K. New Dinuclear Lanthanide(III) Complexes Based on 6,6,7,7,8,8,8-Heptafluoro-2,2-Dimethyl-3,5-Octanedione and 2,2′-Bipyrimidine. *Inorg. Chem. Commun.* **2009**, *12*, 296−299.
(79) Irfanullah, M.; Iftikhar, K. New Hetero-Dilanthanide Complexes Containing $Ln^1(fod)_3$ and $Ln^2(fod)_3$ Fragments (Ln=Pr-Nd; Nd-Sm; Eu-Tb and Ho-Er) Linked by Bis-Diimine Bridging Ligand. *Inorg. Chem. Commun.* **2010**, *13*, 694−698.
(80) Binnemans, K. Interpretation of Europium(III) Spectra. *Coord. Chem. Rev.* **2015**, *295*, 1−45.
(81) Lo, W.-S.; Zhang, J.; Wong, W.-T.; Law, G.-L. Highly Luminescent Sm^{III} Complexes with Intraligand Charge-Transfer Sensitization and the Effect of Solvent Polarity on Their Luminescent Properties. *Inorg. Chem.* **2015**, *54*, 3725−3727.
(82) Villata, L. S.; Wolcan, E.; Féliz, M. R.; Capparelli, A. L. Solvent Quenching of the $^5D_0 \rightarrow {}^7F_2$ Emission of Eu(6,6,7,7,8,8,8-Heptafluoro-2,2-Dimethyl-3,5-Octanedionate)3. *J. Photochem. Photobiol., A* **1998**, *115*, 185−189.
(83) de Mesquita, M. E.; Júnior, S. A.; Júnior, N. B. C.; Freire, R. O.; e Silva, F. R. G.; de Sá, G. F. Synthesis, Sparkle Model, Intensity Parameters and Spectroscopic Studies of the New $Eu(Fod)_3$phen-NO Complex. *J. Solid State Chem.* **2003**, *171*, 183−188.
(84) Bassett, A. P.; Magennis, S. W.; Glover, P. B.; Lewis, D. J.; Spencer, N.; Parsons, S.; Williams, R. M.; De Cola, L.; Pikramenou, Z. Highly Luminescent, Triple- and Quadruple-Stranded, Dinuclear Eu, Nd, and Sm(III) Lanthanide Complexes Based on Bis-Diketonate Ligands. *J. Am. Chem. Soc.* **2004**, *126*, 9413−9424.
(85) Li, Z.; Yu, J.; Zhou, L.; Zhang, H.; Deng, R. The Optical Properties and the Natural Lifetime Calculation of a Sm(III) Complex. *Inorg. Chem. Commun.* **2008**, *11*, 1284−1287.
(86) Chen, X. Y.; Jensen, M. P.; Liu, G. K. Analysis of Energy Level Structure and Excited-State Dynamics in a Sm^{3+} Complex with Soft-Donor Ligands: $Sm(Et_2\ Dtc)_3$ (Bipy). *J. Phys. Chem. B* **2005**, *109*, 13991−13999.
(87) Stanley, J. M.; Chan, C. K.; Yang, X.; Jones, R. A.; Holliday, B. J. Synthesis, X-Ray Crystal Structure and Photophysical Properties of

https://doi.org/10.1021/acsomega.0c05976
ACS Omega 2021, 6, 21207−21226

Tris(Dibenzoylmethanido)(1,10-Phenanthroline)Samarium(III). *Polyhedron* **2010**, *29*, 2511−2515.
(88) dos Santos, E. R.; Freire, R. O.; da Costa, N. B., Jr.; Paz, F. A. A.; de Simone, C. A.; Júnior, S. A.; Araújo, A. A. S.; Nunes, L. A. O.; de Mesquita, M. E.; Rodrigues, M. O. Theoretical and Experimental Spectroscopic Approach of Fluorinated Ln^{3+}−*β*-Diketonate Complexes. *J. Phys. Chem. A* **2010**, *114*, 7928−7936.
(89) Dutra, J. D. L.; Bispo, T. D.; Freire, R. O. LUMPAC Lanthanide Luminescence Software: Efficient and User Friendly. *J. Comput. Chem.* **2014**, *35*, 772−775.
(90) Leal, J. P.; Outis, M.; Casimiro, M. H.; Ferreira, L. M.; Fernandes, F.; Monteiro, B.; Laia, C. A. T.; Pereira, C. C. L. A Case of Self-Organization in Highly Emissive Eu^{III} Ionic Liquids. *Eur. J. Inorg. Chem.* **2017**, *2017*, 3429−3434.
(91) Kai, J.; Felinto, M. C. F. C.; Nunes, L. A. O.; Malta, O. L.; Brito, H. F. Intermolecular Energy Transfer and Photostability of Luminescence-Tuneable Multicolour PMMA Films Doped with Lanthanide-*β*-Diketonate Complexes. *J. Mater. Chem.* **2011**, *21*, 3796−3802.
(92) Hasan, N.; Iftikhar, K. Synthesis, Crystal Structure and Photoluminescence Studies of $[Eu(dbm)_3(Impy)]$ and Its Polymer-Based Hybrid Film. *New J. Chem.* **2019**, *43*, 2479−2489.
(93) Ilmi, R.; Iftikhar, K. Structure Elucidation by Sparkle/RM1, Effect of Lanthanide Contraction and Photophysical Properties of Lanthanide(III) Trifluoroacetylacetonate Complexes with 1,10-Phenanthroline. *J. Photochem. Photobiol., A* **2016**, *325*, 68−82.
(94) Ilmi, R.; Iftikhar, K. Optical Emission Studies of New Europium and Terbium Dinuclear Complexes with Trifluoroacetylacetone and Bridging Bipyrimidine. Fast Radiation and High Emission Quantum Yield. *Polyhedron* **2015**, *102*, 16−26.
(95) Ilmi, R.; Iftikhar, K. Photophysical properties of Lanthanide-(III) 1,1,1-trifluoro-2,4-pentanedione complexes with 2,2′-Bipyridyl: An experimental and theoretical investigation. *J. Photochem. Photobiol., A* **2017**, *333*, 142−155.
(96) Dar, W. A.; Ganaie, A. B.; Iftikhar, K. Synthesis and Photoluminescence Study of Two New Complexes $[Sm(Hfaa)_3(Impy)_2]$ and $[Eu(Hfaa)_3(Impy)_2]$ and Their PMMA Based Hybrid Films. *J. Lumin.* **2018**, *202*, 438−449.
(97) Dar, W. A.; Iftikhar, K. Phase Controlled Colour Tuning of Samarium and Europium Complexes and Excellent Photostability of Their PVA Encapsulated Materials. Structural Elucidation, Photophysical Parameters and the Energy Transfer Mechanism in the Eu^{3+} Complex by Sparkle/PM3 Calculations. *Dalton Trans.* **2016**, *45*, 8956−8971.
(98) Werts, M. H. V.; Jukes, R. T. F.; Verhoeven, J. W. The Emission Spectrum and the Radiative Lifetime of Eu^{3+} in Luminescent Lanthanide Complexes. *Phys. Chem. Chem. Phys.* **2002**, *4*, 1542−1548.
(99) Carnall, W. T.; Fields, P. R.; Rajnak, K. Electronic Energy Levels of the Trivalent Lanthanide Aquo Ions. IV. Eu^{3+}. *J. Chem. Phys.* **1968**, *49*, 4450−4455.
(100) Carnall, W. T.; Crosswhite, H.; Crosswhite, H. M. *Energy Level Structure and Transition Probabilities in the Spectra of the Trivalent Lanthanides in* LaF_3; Argonne, IL (United States), 1978.
(101) Kodaira, C. A.; Brito, H. F.; Malta, O. L.; Serra, O. A. Luminescence and Energy Transfer of the Europium (III) Tungstate Obtained via the Pechini Method. *J. Lumin.* **2003**, *101*, 11−21.
(102) Ferhi, M.; Bouzidi, C.; Horchani-Naifer, K.; Elhouichet, H.; Ferid, M. Judd-Ofelt Analysis of Spectroscopic Properties of Eu^{3+} doped $KLa(PO_3)_4$. *J. Lumin.* **2015**, *157*, 21−27.
(103) de Sá, G. F.; Malta, O. L.; de Mello Donegá, C.; Simas, A. M.; Longo, R. L.; Santa-Cruz, P. A.; da Silva, E. F., Jr. Spectroscopic Properties and Design of Highly Luminescent Lanthanide Coordination Complexes. *Coord. Chem. Rev.* **2000**, *196*, 165−195.
(104) Walsh, B. M. Judd-Ofelt Theory: Principles and Practices. In *Advances in Spectroscopy for Lasers and Sensing*; Springer Netherlands: Dordrecht, 2006; pp. 403−433.
(105) Jiang, H. D.; Wang, J. Y.; Zhang, H. J.; Hu, X. B.; Liu, H. Optical-Transition Properties of the Nd^{3+} Ion in $Gd_{0.8}$ $La_{0.2}$ VO_4 Crystal. 2007, *3647* (2002), 3647−3650, DOI: 10.1063/1.150568.
(106) Springer, C. S., Jr.; Meek, D. W.; Sievers, R. E. Rare Earth Chelates of 1,1,1,2,2,3,3-Heptafluoro-7,7-Dimethyl-4,6-Octanedione. *Inorg. Chem.* **1967**, *6*, 1105−1110.
(107) Iftikhar, K.; Sayeed, M.; Ahmad, N. Mixed-Ligand Complexes of Trivalent Lanthanide Ions with *β*-Diketones and Heterocyclic Amines. *Inorg. Chem.* **1982**, *21*, 80−84.
(108) Iftikhar, K.; Malik, A. U.; Ahmad, N. Mixed-Ligand Complexes of Trivalent Lanthanides. Part 3. Complexes of Heptafluorodimethyloctane-3,5-Dione and Pyrazine: Syntheses and Spectral Studies. *J. Chem. Soc. Dalton Trans.* **1985**, *12*, 2547.
(109) Ahmed, Z.; Dar, W. A.; Iftikhar, K. Syntheses and Spectroscopic Studies of Volatile Low Symmetry Lanthanide(III) Complexes with Monodentate 1*H*-Indazole and Fluorinated *β*-Diketone. *J. Coord. Chem.* **2012**, *65*, 3932−3948.
(110) Ruminski, R. R.; Johnson, J. O. Synthesis and Characterization of Molybdenum Tetracarbonyl Bound to the Novel Bridging Ligand 2,3-Bis(2-Pyridyl)Pyrazine. *Inorg. Chem.* **1987**, *26*, 210−212.
(111) Armentano, D.; de Munno, G.; Guerra, F.; Faus, J.; Lloret, F.; Julve, M. 2,2′-Bipyrimidine- and 2,3-Bis(2-Pyridyl)Pyrazine-Containing Manganese(II) Compounds: Structural and Magnetic Properties. *Dalton Trans.* **2003**, 4626−4634.
(112) Pereira, V. M.; Costa, A. L.; Feldl, J.; Maria, T. M. R.; Seixas de Melo, J. S.; Martín-Ramos, P.; Martín-Gil, J.; Ramos Silva, M. Synthesis, Structure and Physical Properties of Luminescent Pr(III) *β*-Diketonate Complexes. *Spectrochim. Acta, Part A* **2017**, *172*, 25−33.
(113) Tayyari, S. F.; Vakili, M.; Nekoei, A.-R.; Rahemi, H.; Wang, Y. A. Vibrational Assignment and Structure of Trifluorobenzoylacetone. *Spectrochim. Acta, Part A* **2007**, *66*, 626−636.
(114) Eliseeva, S. V.; Kotova, O. V.; Gumy, F.; Semenov, S. N.; Kessler, V. G.; Lepnev, L. S.; Bünzli, J.-C. G.; Kuzmina, N. P. Role of the Ancillary Ligand *N*,*N*-Dimethylaminoethanol in the Sensitization of Eu^{III} and Tb^{III} Luminescence in Dimeric *β*-Diketonates. *J. Phys. Chem. A* **2008**, *112*, 3614−3626.
(115) Chen, J.; Xing, X.; Rey-de-Castro, R.; Rabitz, H. Ultrafast Photofragmentation of $Ln(Hfac)_3$ with a Proposed Mechanism for Forming High Mass Fluorinated Products. *Sci. Rep.* **2020**, *10*, 7066.
(116) Walker, N.; Stuart, D. An Empirical Method for Correcting Diffractometer Data for Absorption Effects. *Acta Crystallogr., Sect. A: Found. Crystallogr.* **1983**, *39*, 158−166.
(117) Sheldrick, G. M. *SHELXT* - Integrated Space-Group and Crystal-Structure Determination. *Acta Crystallogr., Sect. A: Found. Crystallogr.* **2015**, *71*, 3−8.
(118) Dolomanov, O. V.; Bourhis, L. J.; Gildea, R. J.; Howard, J. A. K.; Puschmann, H. *OLEX2*: A Complete Structure Solution, Refinement and Analysis Program. *J. Appl. Crystallogr.* **2009**, *42*, 339−341.
(119) Sheldrick, G. M. Crystal Structure Refinement with SHELXL. *Acta Crystallogr., Sect. C: Struct. Chem.* **2015**, *71*, 3−8.
(120) Farrugia, L. J. *WinGX* and *ORTEP* for Windows: An Update. *J. Appl. Crystallogr.* **2012**, *45*, 849−854.
(121) Martín-Ramos, P.; Ramos Silva, M.; Lahoz, F.; Martín, I. R.; Chamorro-Posada, P.; Eusebio, M. E. S.; Lavín, V.; Martín-Gil, J. Highly Fluorinated Erbium(III) Complexes for Emission in the C-Band. *J. Photochem. Photobiol., A* **2014**, *292*, 16−25.
(122) Stewart, J. J. P. *MOPAC2016*; Stewart Computational Chemistry, Colorado Springs, CO, USA.
(123) Allouche, A.-R. Gabedit-A Graphical User Interface for Computational Chemistry Softwares. *J. Comput. Chem.* **2011**, *32*, 174−182.

https://doi.org/10.1021/acsomega.0c05976
ACS Omega 2021, 6, 21207−21226